

BIOENGINEERING

Biocompatible near-infrared quantum dots delivered to the skin by microneedle patches record vaccination

Kevin J. McHugh^{1*†}, Lihong Jing^{1,2*}, Sean Y. Severt¹, Mache Cruz¹, Morteza Sarmadi^{1,3}, Hapuarachchige Surangi N. Jayawardena^{1‡}, Collin F. Perkinson⁴, Fridrik Larusson⁵, Sviatlana Rose¹, Stephanie Tomasic¹, Tyler Graf¹, Stephany Y. Tzeng^{1§}, James L. Sugarman¹, Daniel Vlastic⁶, Matthew Peters⁵, Nels Peterson⁵, Lowell Wood⁵, Wen Tang¹, Jihyeon Yeom¹, Joe Collins¹, Philip A. Welkhoff⁷, Ari Karchin⁵, Megan Tse¹, Mingyuan Gao², Mounqi G. Bawendi⁴, Robert Langer^{1||}, Ana Jaklenec^{1||}

Accurate medical recordkeeping is a major challenge in many low-resource settings where well-maintained centralized databases do not exist, contributing to 1.5 million vaccine-preventable deaths annually. Here, we present an approach to encode medical history on a patient using the spatial distribution of biocompatible, near-infrared quantum dots (NIR QDs) in the dermis. QDs are invisible to the naked eye yet detectable when exposed to NIR light. QDs with a copper indium selenide core and aluminum-doped zinc sulfide shell were tuned to emit in the NIR spectrum by controlling stoichiometry and shelling time. The formulation showing the greatest resistance to photobleaching after simulated sunlight exposure (5-year equivalence) through pigmented human skin was encapsulated in microparticles for use in vivo. In parallel, microneedle geometry was optimized in silico and validated ex vivo using porcine and synthetic human skin. QD-containing microparticles were then embedded in dissolvable microneedles and administered to rats with or without a vaccine. Longitudinal in vivo imaging using a smartphone adapted to detect NIR light demonstrated that microneedle-delivered QD patterns remained bright and could be accurately identified using a machine learning algorithm 9 months after application. In addition, codelivery with inactivated poliovirus vaccine produced neutralizing antibody titers above the threshold considered protective. These findings suggest that intradermal QDs can be used to reliably encode information and can be delivered with a vaccine, which may be particularly valuable in the developing world and open up new avenues for decentralized data storage and biosensing.

INTRODUCTION

Vaccines are exceptionally safe and effective, saving an estimated 2 million to 3 million lives annually (1). However, each year, 1.5 million vaccine-preventable deaths occur due to undervaccination—primarily in areas of the developing world with poor health care infrastructure (2). One key barrier to improving vaccination coverage in these regions is the inability to accurately identify the immunization status of infants given resource constraints, which can affect the quality of care provided (3, 4). These areas often lack accurate medical recordkeeping systems and rely on vaccination campaigns to distribute vaccines. However, investigations in response to recent

outbreaks of measles and mumps in the United States (5), Australia (6), and Italy (7) have highlighted that poor immunization record-keeping is not unique to developing nations.

Paper vaccination cards or certificates are the most widely used records in the developing world but are subject to error (8) and possessed by only 60% of all households in low- and middle-income countries (9). Without accurate vaccination records, health care professionals lack the data needed to make informed decisions about administering vaccines, often relying on parental recall (10). This may result in the application of additional, unnecessary vaccine doses and therefore undue cost or, more problematically, missed opportunities to vaccinate, which leave the child at risk for contracting infectious diseases (8, 10). As many as two-thirds of opportunities to vaccinate may be missed in some areas (11), leading to a potential 30% drop in vaccination coverage (3). Several solutions have been proposed including smartphone-based database applications (12), fingerprinting (13), and near-field communication chips (14); however, these more technologically advanced methods have yet to achieve widespread adoption due to difficulty of implementation.

Therefore, we aimed to develop a platform that is robust, inexpensive, and easy to use to overcome the primary obstacles to implementation in the developing world. We hypothesized that information, such as vaccination history, could be encoded invisibly in the skin by applying a distinct pattern of near-infrared (NIR) fluorescent microparticles using a microneedle patch. By providing all of the requisite information on the patients themselves and delivering microparticles in the same microneedles as the vaccine, this platform offers several key advantages compared to traditional

¹Koch Institute for Integrative Cancer Research, Massachusetts Institute of Technology, 77 Massachusetts Avenue, Cambridge, MA 02139, USA. ²Key Laboratory of Colloid, Interface and Chemical Thermodynamics, Institute of Chemistry, Chinese Academy of Sciences, Bei Yi Jie 2, Zhong Guan Cun, Beijing 100190, China. ³Department of Mechanical Engineering, Massachusetts Institute of Technology, 77 Massachusetts Avenue, Cambridge, MA 02139, USA. ⁴Department of Chemistry, Massachusetts Institute of Technology, 77 Massachusetts Avenue, Cambridge, MA 02139, USA. ⁵Global Good, Intellectual Ventures Laboratory, 14360 SE Eastgate Way, Bellevue, WA 98007, USA. ⁶Independent consultant, 119 Kendall Rd, Lexington, MA 02421, USA (<https://people.csail.mit.edu/draniel/>). ⁷Institute for Disease Modeling, 3150 139th Ave. SE, Bellevue, WA 98005, USA.

*These authors contributed equally to this work.

†Present address: Department of Bioengineering, Rice University, Houston, TX 77005, USA.

‡Present address: Department of Chemistry, University of Alabama in Huntsville, Huntsville, AL 35899, USA.

§Present address: School of Medicine, Johns Hopkins University, 733 N. Broadway, Baltimore, MD 21205, USA.

||Corresponding author. Email: rlanger@mit.edu (R.L.); jaklenec@mit.edu (A.J.)

paper or electronic medical records including the following: (i) the elimination of reliance on widely accessible, yet secure database of patient information; (ii) lack of reliance on accurate patient identification and data entry by medical professionals; (iii) ability to make rapid determinations of vaccination status; (iv) elimination of vaccination fraud; (v) capacity for population-level assessment of vaccine coverage; and (vi) minimal cost that is feasible to implement in low-resource settings. By using a microneedle form factor, this platform should easily assimilate into the future vaccination landscape because microneedles are currently in development for several vaccines (15) and have shown advantages such as antigen dose sparing, improved antigen stability, and ease of (self-)administration compared to traditional soluble injections (16–18). Microneedle patches for vaccination recordkeeping may not require cold chain storage and could potentially have long shelf life, which could greatly enhance feasibility of implementation in low-resource settings.

RESULTS

Commercial dye and custom quantum dot characterization

To create a microneedle platform that could be applied to the skin, rapidly dissolve, and leave behind particles that can later be imaged to determine vaccination status (Fig. 1, A to C), we first needed to identify a suitable candidate for long-term detection. We began by investigating the use of commercial fluorophores with emission in the NIR spectrum (fig. S1). To examine resistance to photobleaching, a key criterion for use in our application, fluorescent dyes were covered with pigmented cadaveric human skin and exposed to light simulating the solar spectrum at sevenfold higher intensity. Despite being heavily protected from light by overlying human skin, organic fluorophores photobleached within a few weeks of simulated sun exposure (Fig. 1D). Alternatively, inorganic commercial dyes demonstrated considerable resistance to photobleaching but exhibited low fluorescence intensity per mass and were difficult to process because of their insolubility in both water and organic solvents. We then pursued the use of colloidal quantum dots (QDs), also known as semiconductor nanocrystals, as potential fluorescent probes due to their favorable brightness and photostability. We synthesized and characterized more than 60 distinct combinations of copper indium selenide cores and ZnS:Al shells (table S1). By changing the core stoichiometry and shell thickness, we could control the peak emission wavelength (Fig. 1E), enhance the photoluminescence quantum yield (PL QY) (Fig. 1F), and affect other optical properties (figs. S2 and S3 and table S2). For example, in one QD formulation, performing the shelling process for 5 hours resulted in an increase PL QY from 16.2 to 43.6% and a blue shift in the emission peak from 964 to 891 nm.

We then selected five QD formulations with emission peaks ranging from 828 to 891 nm to optimize *in vivo* light transmission and detection (Fig. 1G). These QDs were exposed to simulated solar light through pigmented cadaveric skin at sevenfold the intensity of the sun for a period that simulated 5 years of day/night exposure. One QD formulation, S10C5H, demonstrated substantially greater resistance to photobleaching than other formulations ($P < 0.05$), retaining $13 \pm 3\%$ of signal after five simulated years compared to the next best candidate, which retained only $4 \pm 2\%$ of its initial signal (Fig. 1H). This represented about 50-fold improvement in resistance to photobleaching compared to the top-performing organic

dyes tested. As a result, S10C5H was chosen for subsequent experiments. These QDs were 3.7 ± 0.6 nm in diameter and displayed the chalcopyrite phase structure characteristic of bulk CuInSe₂ (Fig. 1I and fig. S4).

QD encapsulation

After synthesis, a subset of S10C5H QDs was encapsulated in poly(methyl methacrylate) (PMMA) microspheres using a spontaneous emulsion/solvent evaporation technique (Fig. 2, A to D). Emulsion parameters such as surfactant concentration and homogenization speed were refined to produce particles that contained 60% QDs by mass with an average size of 15.7 ± 5.3 μm (Fig. 2E). Encapsulated QDs displayed a similar but slightly red-shifted emission peak due to Förster resonance energy transfer in closely packed QDs (Fig. 2F). Despite the about 40% loss of signal per mass due to the presence of PMMA, these particles still exhibited bright fluorescence (Fig. 2G), which was stable for months in phosphate-buffered saline (PBS) at 37°C (Fig. 2H). QDs embedded in PMMA also demonstrated consistent fluorescence intensity over a pH range that would be physiologically relevant in the phagolysosome (fig. S5).

Microneedle geometry optimization

To determine the optimal microneedle geometry for this application, finite element analysis was performed. Fifty shapes ranging from a cone to a cylinder at a fixed height of 1500 μm were mechanically analyzed to ensure deep delivery of QDs into a permanent (nonshedding) layer of skin (figs. S6 and S7). Important design criteria were to provide ample resistance to mechanical failure while also achieving a high deliverable volume, defined as the volume near the dissolving microneedle tip. Finite element analysis identified that microneedles with diameters of 100 or 200 μm were prone to failure due to both bending and axial loading; therefore, all subsequent studies used needles 300 μm in diameter. Both the mechanical performance and the deliverable volume from the needles were heavily dependent on α (the proportion of microneedle height that was cylindrical) (Fig. 3 and figs. S6 and S7). Increasing α generally contributed to higher deliverable drug volume, improved buckling resistance, and decreased maximum stress and displacement under axial loading while increasing maximum stress under bending. From these simulations, a value of 0.5 was selected for α . The maximum von Mises stress for our chosen microneedle geometry under bending and axial loading were 9.46 and 8.71 MPa, respectively; the axial and bending displacement were found to be negligible, and the critical load factor was 0.0146 (fig. S6). After considering these factors along with deliverable volume, a microneedle with a 300- μm -wide cylindrical base that was 750 μm in height with an upper cone 750 μm in height was selected as a leading candidate for further study.

To verify *in silico* modeling data, we down-selected to three 3×3 arrays of microneedles: A 1500- μm cone (Fig. 3, A and B), a 750/750- μm cylinder/cone (Fig. 3, C and D), and a 1250/250- μm cylinder/cone (Fig. 3, E and F) were printed using two-photon polymerization to create a master mold in photoresist. These shapes were maintained when the photoresist masters were used to produce inverse polydimethylsiloxane (PDMS) molds and ultimately positive dissolvable microneedles composed of poly(vinyl alcohol) and sucrose (Fig. 3G).

The force required to penetrate synthetic human skin or explanted pig skin with nondegradable *in silico*-optimized needles

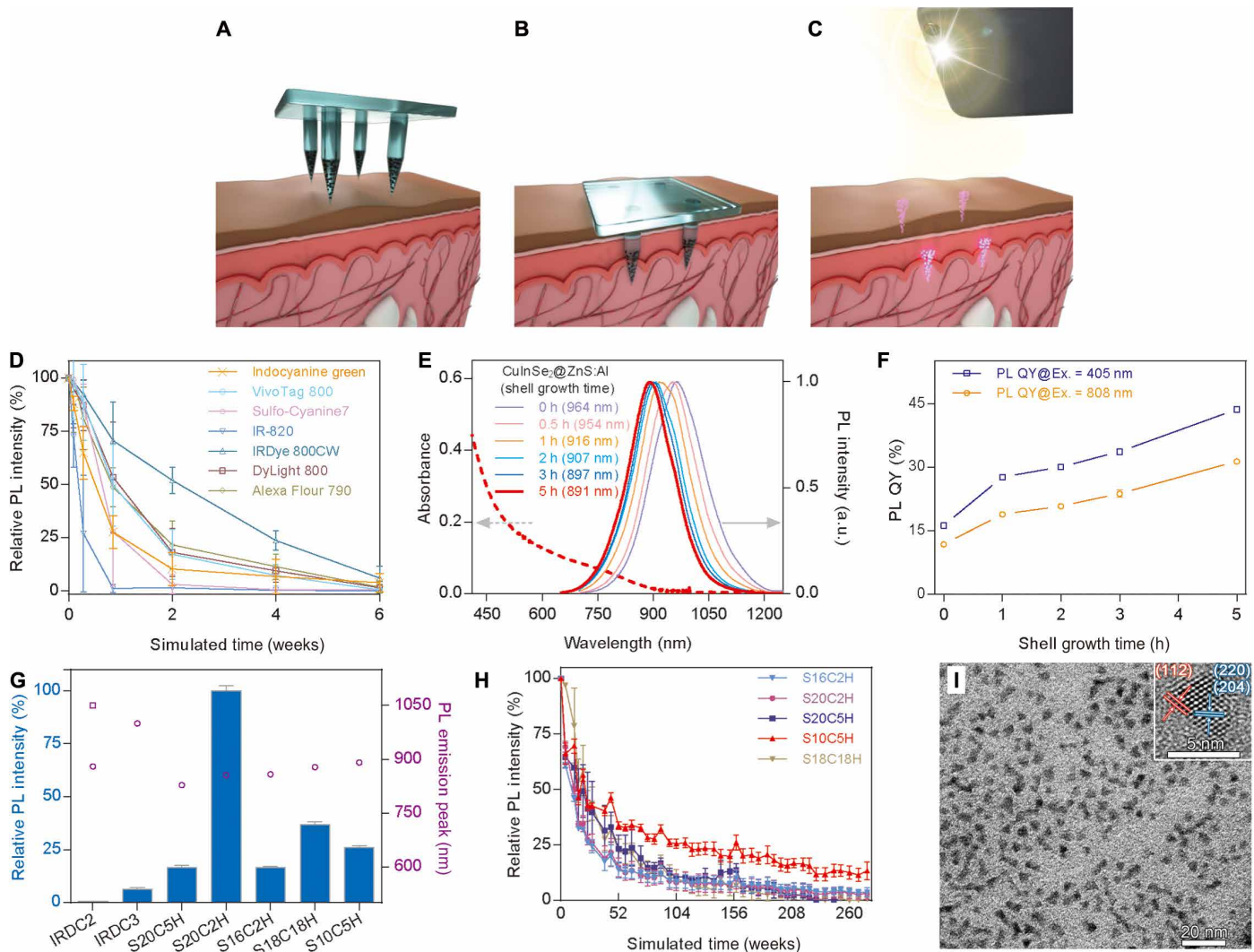


Fig. 1. Platform schematic and fluorescent probe characterization. (A) Fluorescent microparticles are distributed through an array of dissolvable microneedles in a distinct spatial pattern. (B) Microneedles are then applied to the skin for 2 to 5 min, resulting in dissolution of the microneedle matrix and retention of fluorescent microparticles. (C) A NIR LED and adapted smartphone are used to image patterns of fluorescent microparticles retained within the skin. By selectively embedding microparticles within microneedles used to deliver a vaccine, the resulting pattern of fluorescence detected in the skin can be used as an on-patient record of an individual's vaccination history. (D) Rapid photobleaching of organic dyes covered with pigmented human skin under simulated solar light. (E) Emission profiles of QDs (solid lines) show a blue shift with increased shelling time. Dashed line depicts absorption by the 5-hour shelling sample. Arrows indicate the relevant y axis for absorption (left) and emission (right). a.u., arbitrary units. (F) PL QY as a function of shelling time under different excitation wavelengths. (G) Relative photoluminescence intensity comparison of QDs with the commercial inorganic dyes IRDC2 and IRDC3 (blue bars) and corresponding emission peaks (empty purple circles and square). (H) Photostability of QDs covered with pigmented human skin under simulated solar light. (I) Transmission electron microscopy (TEM) and high-resolution TEM (inset) showing the size and crystal structure of ZnS:Al-coated CuInSe₂ QDs. Scale bars, 20 and 5 nm, respectively. $n = 3$ for all graphs containing error bars. Error bars indicate SD.

(750/750- μm cylinder/cone) was not significantly different from conical needles ($P = 0.46$ and $P = 0.07$, respectively), which have a lower deliverable volume, but substantially less force than the blunter (1250/250- μm cylinder/cone) needles was required (Fig. 3H). Decreasing the spacing of microneedles from 3.23 to 1.57 mm (1 cm by 1 cm and 0.5 cm by 0.5 cm patch sizes, respectively) did not affect the amount of force required for penetration (Fig. 3I). As a result, we confirmed our selection of microneedles with a height of 1500 μm , diameter of 300 μm , and α of 0.5 as the best combination of penetration depth, resistance to mechanical fracture, and maximum capacity for microparticle delivery.

Smartphone imaging system design and ex vivo skin penetration

To enable the imaging of NIR QDs in a field setting, we designed an inexpensive, smartphone-based imaging system. A 780-nm NIR light-emitting diode (LED) was paired with an 800-nm short-pass filter and aspheric condenser with diffuser to excite the QDs (Fig. 4A). For NIR fluorescence detection, a Nexus 5X smartphone (Google) was stripped of its stock short-pass NIR filter and paired with an 850-nm long-pass color glass filter and an 850-nm long-pass dielectric filter set in a poly(lactic acid) three-dimensional (3D)-printed phone case (Fig. 4B). Imaging a QD-loaded microneedle patch with and

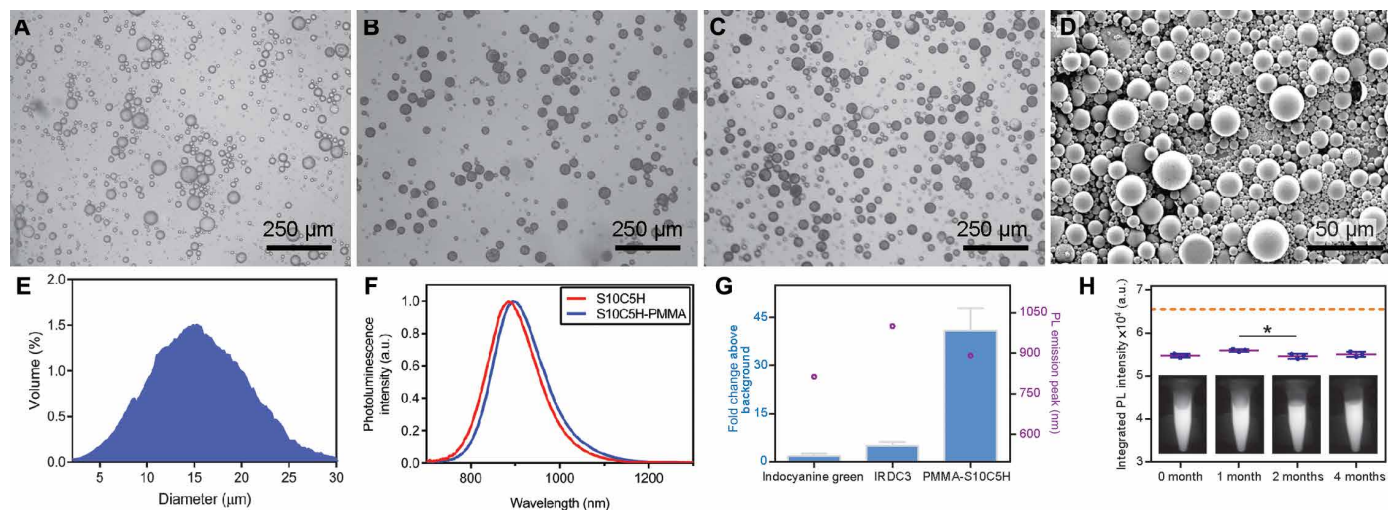


Fig. 2. Encapsulation and characterization of QDs in PMMA microspheres. Light microscopy images of PMMA microspheres loaded with (A) 0% (w/w) QDs, (B) 37.5% (w/w) QDs, and (C) 60% (w/w) QDs. (D) SEM image of PMMA microparticles containing S10C5H QDs. (E) Histogram of volumetric particle distribution smoothed using an 11-frame moving window smoothing function for improved clarity, $n = 10^4$ particles analyzed. (F) Photoluminescence profiles of S10C5H QDs before and after PMMA encapsulation showing a minimal shift in fluorescence emission wavelength. (G) Relative photoluminescence intensities (blue bars) using an 850-nm long-pass filter ($n = 2$) and emission peaks (empty purple circles). (H) Maintenance of photoluminescence intensity in PBS at 37°C over the course of months ($n = 3$), with representative NIR images inlaid at their respective time points; * $P < 0.05$ (one-way ANOVA with Tukey's multiple comparisons). Dashed line indicates the camera saturation point. Error bars indicate SD.

without the long-pass emission filters demonstrated the ability to filter background light while retaining NIR QD signal transmission (Fig. 4, C and D). All imaging was performed under ambient indoor lighting with no measures taken to reduce environmental background.

We then tested the ability of microneedles to deliver fluorescent microparticles into explanted tissue samples. A simple spring-loaded applicator was used to administer microneedles into ex vivo pig skin and human cadaveric skin for a duration of 2 min, in accordance with the optimal wear time identified by the global health organization PATH (19). Before application, microneedles appeared sharp with optically dark tips where QD-loaded microparticles were embedded (Fig. 4, E and F). After application, microneedles were blunted as a result of the partial dissolution of the tip (Fig. 4, G and H). Although many fluorescent microparticles remained within the body of the needle, the transfer of QD-loaded particles from the 4×4 microneedle array into both pig skin (Fig. 4, I to L) and pigmented human skin (Fig. 4, M to P) was obvious when imaged using our NIR-adapted smartphone camera, yet not apparent by naked eye, as intended.

Pattern imaging, manual analysis, and machine learning-based pattern recognition

After confirming penetration and dissolution ex vivo, an 8-day study was performed to assess in vivo delivery. Microneedle patches containing QDs were administered to the rear flank of Wistar rats, as shown in movie S1. Before administration, hair at the application site was removed using an electric razor and depilatory cream. Microneedles were applied using a spring-loaded applicator and held in place for 2 min to allow for partial dissolution. This study revealed the importance of encapsulating QDs to ensure their delivery and prolonged residence in the body. Unencapsulated QDs resulted in very little and inconsistent transfer into the skin, likely due to their hydrophobicity (Fig. 5A). Alternatively, encapsulated QDs showed a much higher transfer of fluorescence into the skin

that resulted in a NIR signal that was 10-fold higher than unencapsulated QDs (Fig. 5B). Over the days after administration, the signal from unencapsulated QDs was no longer apparent after 24 hours, whereas the signal from encapsulated QDs decreased on the first 2 days after application but then seemed to stabilize (Fig. 5C).

Next, to test the longevity of QD-containing PMMA microparticles in vivo, we administered patches containing eight microneedles in one of three distinct patterns—a circle on day 0, a cross on day 28, and a rectangle on day 56—and performed longitudinal imaging over 9 months (Fig. 5, D to I). On the day of application, markings were visible on the skin for 100% of needles (120 of 120) with very high contrast. By the 24-week time point, 92% (110 of 120) remained visible with somewhat lower contrast than on the day of application. The number of marks per pattern at this time was 7.3 ± 0.8 , which was largely independent of the spatial distribution of microneedles at the time of administration (7.4 ± 0.8 , 7.2 ± 0.8 , and 7.4 ± 0.8 for the circle, cross, and rectangle, respectively) (Fig. 5J). Fluorescent marks exhibited an average signal that was 29-, 23-, and 29-fold higher than background at 3, 6, and 9 months after administration, respectively, when considering the aggregate of all patterns (Fig. 5K). There were no statistical differences between the signal at 3 and 6 months ($P = 0.53$), 3 and 9 months ($P = 0.998$), or 6 and 9 months ($P = 0.50$).

Although patterns were easy to manually identify, we aimed to automate this process to improve its ease of implementation and thus potential clinical impact. To eliminate the need for personnel training and minimize opportunities for human error, we developed a machine learning algorithm based on the AlexNet neural network (20) to automatically classify each pattern (fig. S8). Using this neural network, we were able to correctly classify 100% of test image patterns (210 images in total) that were collected biweekly for up to 30 weeks. In addition to correctly classifying all patterns, the probability of those classifications was also very high, with no trend toward lower probabilities over time (Fig. 5L). Of the 210 images

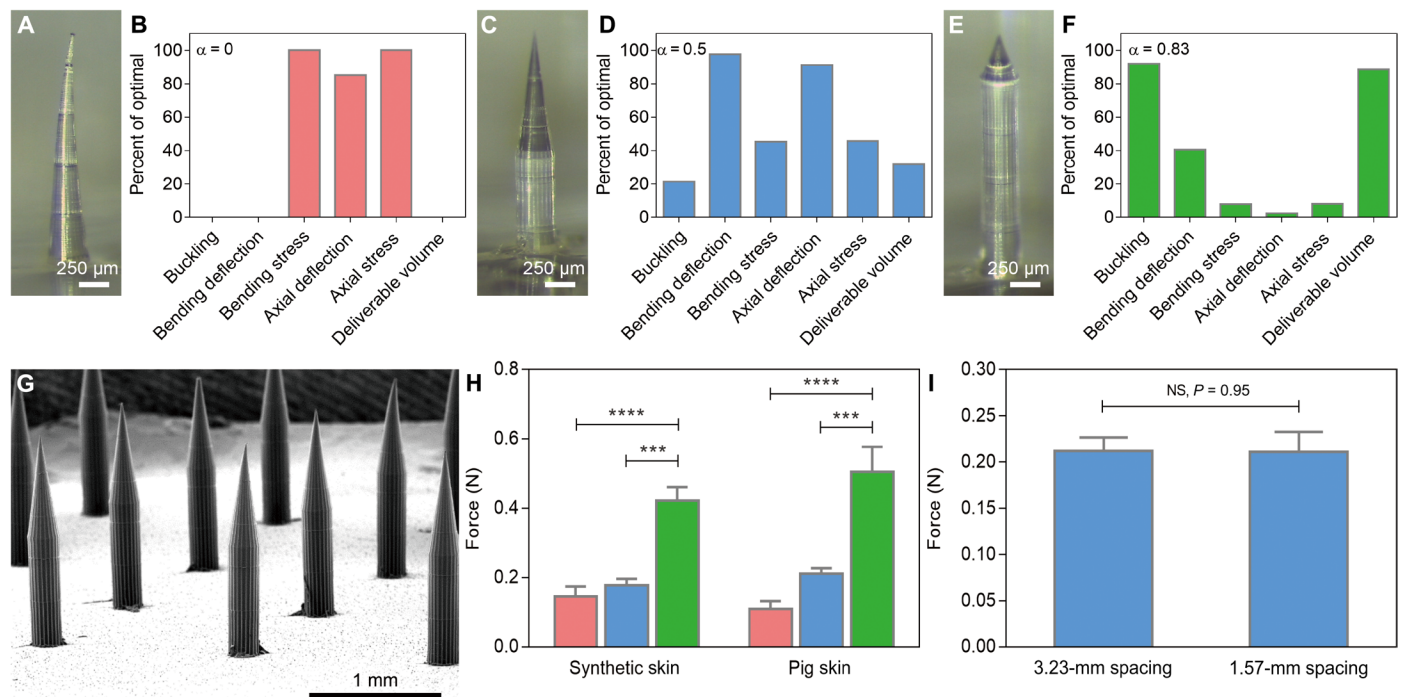


Fig. 3. Microneedle modeling, fabrication, and evaluation. Optical images of microneedles and finite element analysis data of (A and B) a conical needle 1500 μm in height and 300 μm at its base; (C and D) a microneedle 300 μm at its base with a 750- μm cone atop a 750- μm cylinder; and (E and F) a microneedle 300 μm at its base with a 250- μm cone atop a 1250- μm cylinder. (G) SEM image of a dissolvable microneedle array based on the geometry shown in (C). (H) Ex vivo penetration force per needle based on microneedle geometry; $n = 3$; *** $P < 0.001$ and **** $P < 0.0001$ (one-way ANOVA with Tukey's multiple comparisons). (I) Spacing-independent penetration force requirements in pig skin ex vivo (Student's t test). In (B), (D), and (F), 0 and 100 represent the worst and best values, respectively, for each parameter for α between 0 and 1.

analyzed, the lowest classifications probability for image was 98.4% for the cross pattern in one rat on day 154. These data suggest that changes in signal intensity occur soon after administration (within 3 months) but that this does not affect detection reliability. This is also supported by qualitative images shown in Fig. 6 that depict dimmer signals between 0 and 12 weeks but no further substantial losses between 12 and 24 weeks.

QD-loaded microparticle biocompatibility and codelivery with polio vaccine

We then sought to test the in vitro and in vivo biocompatibility of our QDs. In vitro evaluation of cytotoxicity confirmed that our custom QDs composed of CuInSe₂ cores and ZnS:Al shells were less toxic to macrophages than commercially available PbS QDs with a similar oleic acid surface treatment (Fig. 7A). Whereas no dose-dependent toxicity was observed in the range of S10C5H QD concentrations tested, we did observe a trend in PbS QD toxicity with a significant drop in cell viability at 1000 $\mu\text{g}/\text{ml}$ ($P < 0.05$).

Histological examination of the local tissue response revealed tissue damage consistent with needle penetration 1 day after administration (Fig. 7, B and C). A minimal foreign body reaction was observed at 2 weeks (Fig. 7, D and E) and 4 weeks (Fig. 7, F and G). At both later time points, there appeared to be a small number of macrophages and foreign body giant cells at the site of administration. No fibrous encapsulation was observed over the time points collected, supporting the biocompatibility of the microparticles. In general, these results suggest that the PMMA-encapsulated S10C5H QDs largely remain local and are well tolerated by the body. These

observations were in agreement with visual observation of live animals over the days after microneedle administration, which showed no obvious signs of irritation beyond the date of application.

To observe the compatibility of this approach with vaccine delivery, we evaluated the immune response to three doses of microneedle-delivered Salk inactivated poliovirus vaccine type 2 (IPV2) administered at 0, 1, and 2 months with or without QD-loaded microparticles. IPV2 coadministered with microparticles induced total and neutralizing IPV2 antibody titers that were not statistically different ($P = 1.00$ and $P = 0.91$, respectively) from those achieved by IPV2 delivered by microneedles alone (Fig. 7, H and I). Total and neutralizing titers induced by microneedles containing QD-loaded microparticles and IPV2 were also noninferior to three subcutaneous injections of IPV2 ($P = 0.25$ and $P = 0.32$, respectively) despite the use of a suboptimal formulation, suggesting a strong dose-sparing effect because only $25 \pm 2\%$ of the vaccine retained its D-antigenicity during microneedle fabrication and a large fraction of IPV2 remained undelivered within the incompletely dissolved microneedles. Despite the substantially lower dose of antigen delivered in its immunity-conferring conformation, the neutralizing antibodies achieved were well above the threshold considered protective by the U.S. Centers for Disease Control and Prevention (21).

DISCUSSION

To maximize the utility of this technology for vaccination campaigns, we aimed to create a platform compatible with microneedle-delivered vaccines that could reliably encode data on an individual for at least

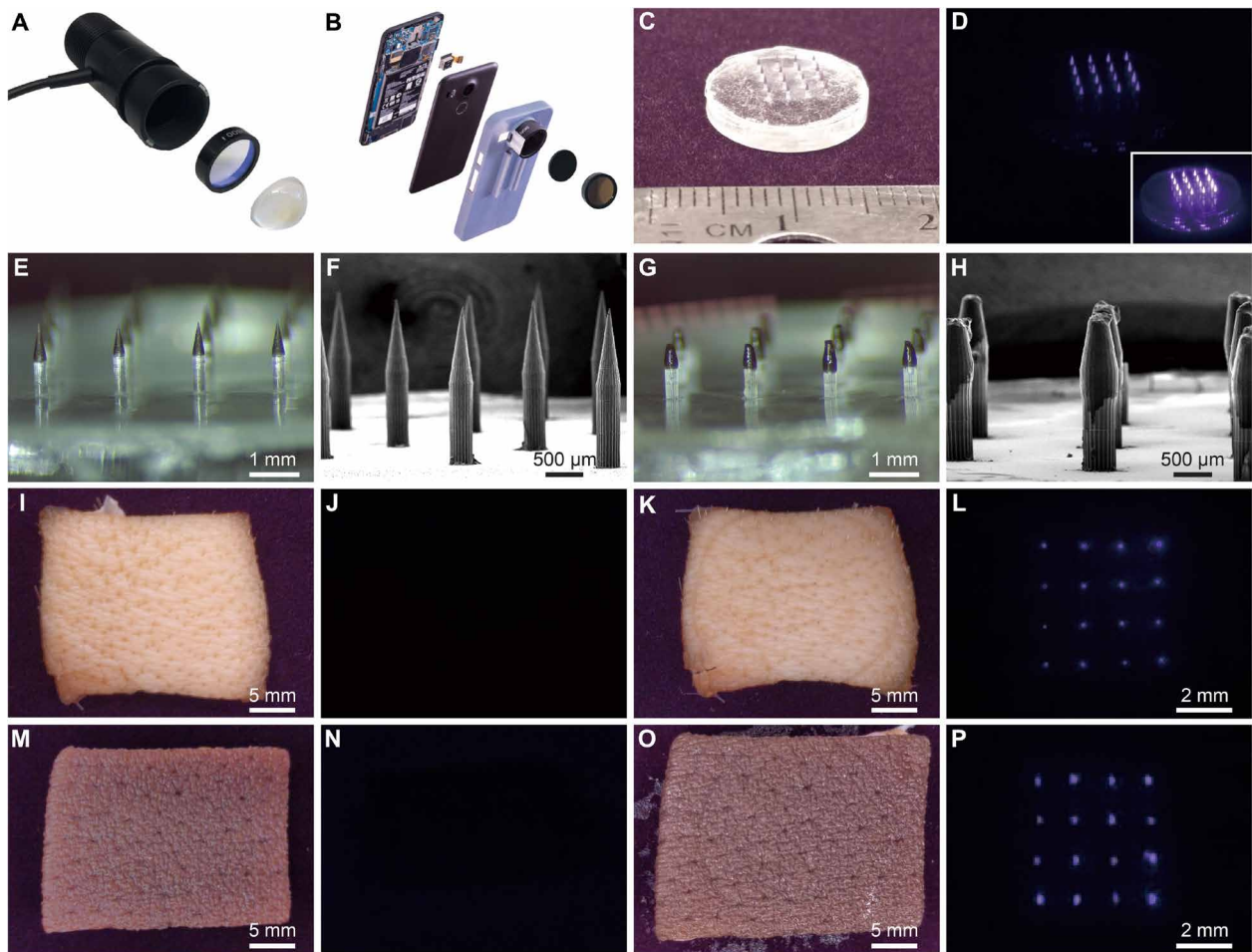


Fig. 4. Smartphone modifications and NIR marking detection in skin. (A) Photograph of disassembled LED used for NIR illumination at 780 nm combined with an 800-nm short-pass filter and aspheric condenser. (B) Photograph of disassembled NIR imaging smartphone consisting of a Google Nexus 5X smartphone with the internal short-pass filter removed and replaced with two external 850-nm long-pass filters set in a 3D-printed phone case. Images of a 16-needle microneedle patch containing PMMA-encapsulated QDs were collected with the adapted smartphone under ambient indoor lighting (C) without the 850-nm long-pass filters and (D) with the pair of 850-nm long-pass filters under LED illumination from the same distance. Inset shows an image at a higher exposure. (E) Optical and (F) SEM images of fluorescent microparticle-loaded microneedles before skin application. (G) Optical and (H) SEM images of microneedles after administration to explanted pig skin. Adapted smartphone images of pig skin before microneedle application (I) without and (J) with 850-nm long-pass filters. Adapted smartphone images of pig skin after application (K) without and (L) with 850-nm long-pass filters. Adapted smartphone images of pigmented human skin before microneedle application (M) without and (N) with the 850-nm long-pass filters. Smartphone images of human skin after application (O) without and (P) with the 850-nm long-pass filters. Note: Scale bars in NIR-filtered images are approximate with (J), (L), (N), and (P) taken at about the same distance. Components in (A) and (B) cropped for clarity.

5 years after administration. In addition, this system also needed to be highly biocompatible, deliver a sufficient amount of dye after an application time of 2 min or less, and be detectable using a minimally adapted smartphone. Given the limitations of organic dyes (photobleaching and water solubility) and inorganic dyes [rare earth metal toxicity (22), low fluorescence, and processing difficulty], QDs were an attractive option as a potentially bright, photostable, and tunable alternative. However, clinical implementation of QDs has been stymied by the toxicity of their core elements, such as cadmium and lead (23). To overcome these safety concerns—which are especially important because these materials would be given to healthy children—we chose to synthesize custom QDs composed of more well-tolerated elements. We identified an optimal fluorescent emission range of 850 to 1100 nm. Operating in this range mitigates the potential cultural opposition to visible skin markings, reduces background from ambient light, minimizes light absorption by tissue at wavelengths

below 850 nm (24), and maximizes signal detection by avoiding the poor sensitivity of inexpensive silicon-based detectors to light above 1100 nm (25). Although the use of fluorophores at the higher end of the NIR-II window (1000 to 1700 nm) would further improve tissue transparency and reduce background (26), appropriate detectors for these wavelengths (indium gallium arsenide) are typically considered cost prohibitive (27), which could render this approach infeasible for widespread implementation.

Fluorophore photobleaching under accelerated solar light exposure enabled us to predict signal loss associated with sun exposure over long periods of time. As expected, organic fluorophores degraded relatively quickly despite protection by heavily pigmented skin, which absorbs a large fraction of ultraviolet (UV) and visible light. These dyes also exhibited strong self-quenching in the dry state and therefore had to be studied in a dispersed, hydrated state. This self-quenching property is problematic for this microneedle-delivered

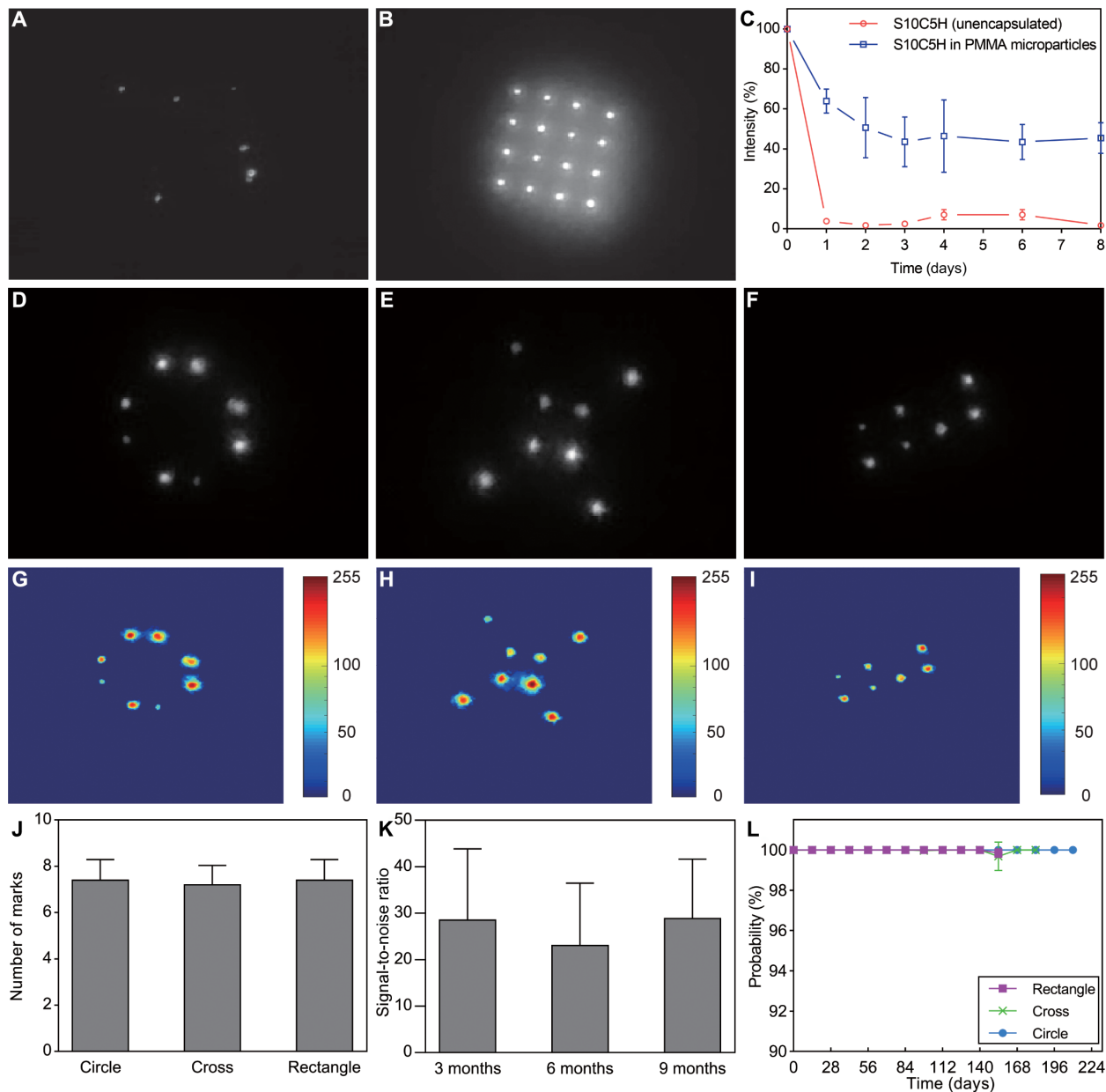


Fig. 5. In vivo imaging of NIR patterns in rodent skin. Administration site after the delivery of a 4×4 microneedle patch containing (A) unencapsulated QDs or (B) PMMA-encapsulated QDs. (C) Short-term study of signal intensity after microneedle application of unencapsulated or PMMA-encapsulated QDs to rat skin, $n = 4$. Images of (D) circle, (E) cross, and (F) rectangle patterns imaged 24 weeks after administration of PMMA-encapsulated QDs to rats. Log-scale color maps of the same (G) circle, (H) cross, and (I) rectangle patterns shown in (D) and (F). (J) Number of markings detected 24 weeks after administration, $n = 5$. (K) Quantification of signal-to-noise ratio for the circle pattern showing no changes between 12, 24, and 36 weeks, $n = 15$ (one-way ANOVA with Tukey's multiple comparisons). (L) Graph showing the average probability of the machine learning algorithm (all patterns correctly detected), $n = 5$. Grayscale images extracted from red channel of the adapted smartphone-generated Red Green Blue (RGB) image.

recording system because it limits the packing density of the dye and thus its brightness. Alternatively, QDs performed very well under light exposure and have a larger Stokes shift, which enables them to avoid substantial reabsorption and therefore be used in a densely packed format.

Although the accelerated photobleaching assay does not perfectly mimic the real-world use case, it does provide evidence supporting the longevity of QDs compared to organic dyes. Further, this experimental setup may overestimate photobleaching because it assumes

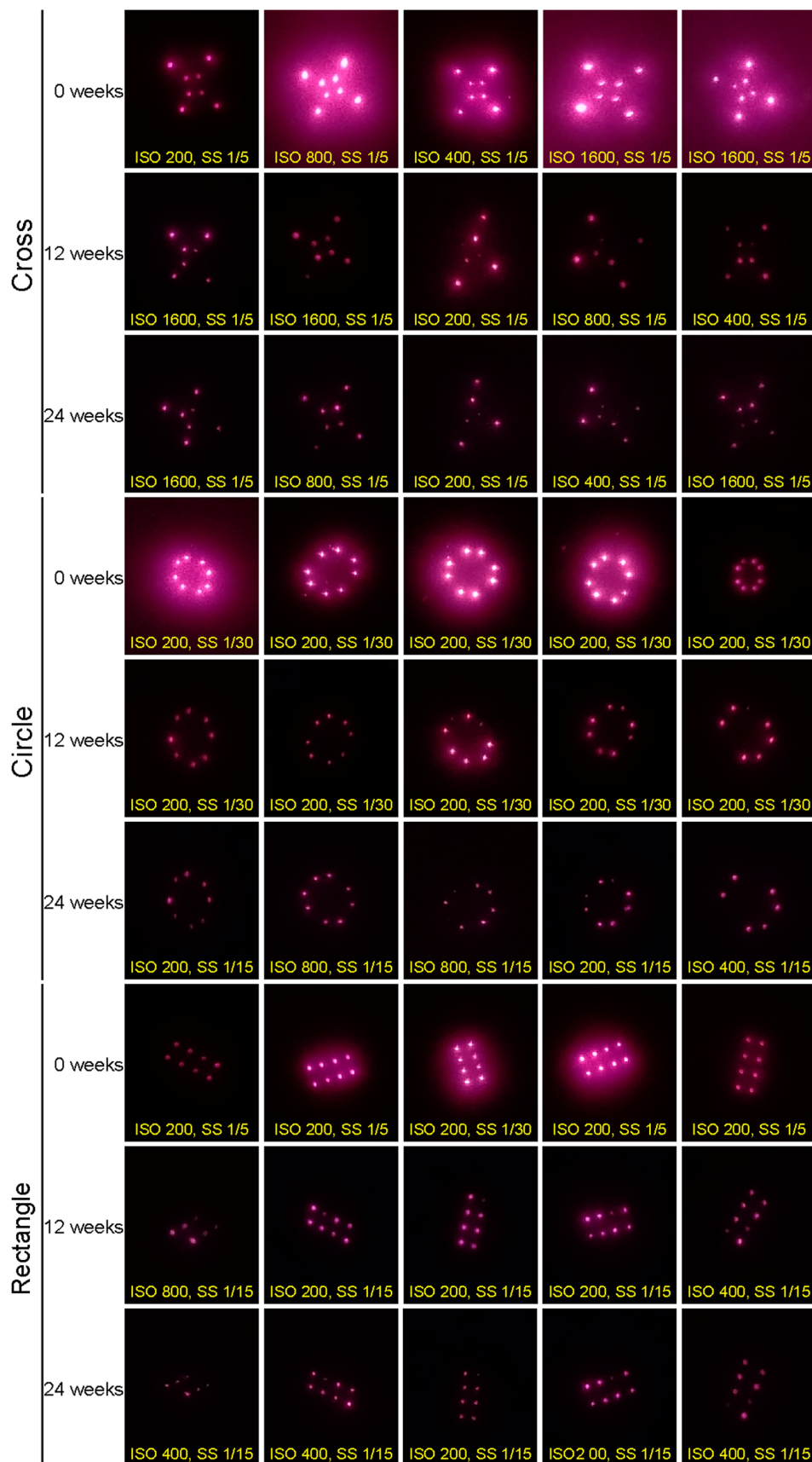
that skin is in direct sunlight every hour of the day that the sun is out. If administered at the thigh, where current vaccines are administered to infants, this area may be covered by clothing and/or in an area that is not exposed to direct sunlight for some portion of the daytime. In addition, photobleaching may also be enhanced in this experiment because sevenfold more intense light results in greater energy transfer per time, potentially enabling QD degradation to proceed more quickly.

PMMA was used as a nondegrading, encapsulating material for QDs to improve biocompatibility and enhance tissue permanence.

Fig. 6. Longitudinal imaging of NIR markings in rodent skin. Cropped, but otherwise raw, smartphone images collected from a fixed distance showing the intradermal NIR signal from PMMA-encapsulated QDs delivered via microneedle patches on rats 0, 12, and 24 weeks after administration. The text at the bottom of each image indicates the image collection settings ISO density and shutter speed (SS) in seconds.

The large size of microparticles ($15.7 \pm 5.3 \mu\text{m}$) was also hypothesized to minimize clearance because previous studies have shown that larger particles are more resistant to clearance by macrophages, the most relevant cell type for clearing foreign material (28). The flexibility of QD surface coating also enabled us to make QDs soluble in the same organic solvent as PMMA, which helped markedly enhance loading given that a traditional double emulsion technique (water-in-oil-in-water) cannot achieve 60% (w/w) loading.

We hypothesized that, unlike microneedle-delivered vaccines, which must simply break the skin's water barrier to deliver their payload effectively (29), these fluorescent microparticles must be delivered below the shed layers of skin to ensure their long-term residence in tissue. Therefore, we aimed to create needles 1500 μm in length. To successfully penetrate to this depth, the microneedles must resist mechanical stress, deflection, and displacement upon insertion into skin. To effectively deliver PMMA-encapsulated QDs into the skin, the microneedles must pierce the skin without fracturing. The critical load factor of 0.014557 was higher than the values reported for carboxymethyl cellulose microneedles using the same simulation procedures (30). The final selection of $\alpha = 0.5$, height = 1500 μm , and width = 300 μm avoids critically low mechanical robustness against all the major mechanisms of mechanical failure. Using a larger diameter and larger α increased the volume of material and thereby the number of QD-loaded particles that are available for transfer into the skin. The drawback of this is the potential increase in pain and higher penetration force requirements. However, although pain perception has been shown to increase with the diameter of hypodermic needles (31–33), the amount of pain induced by our microneedle patch is likely less than for



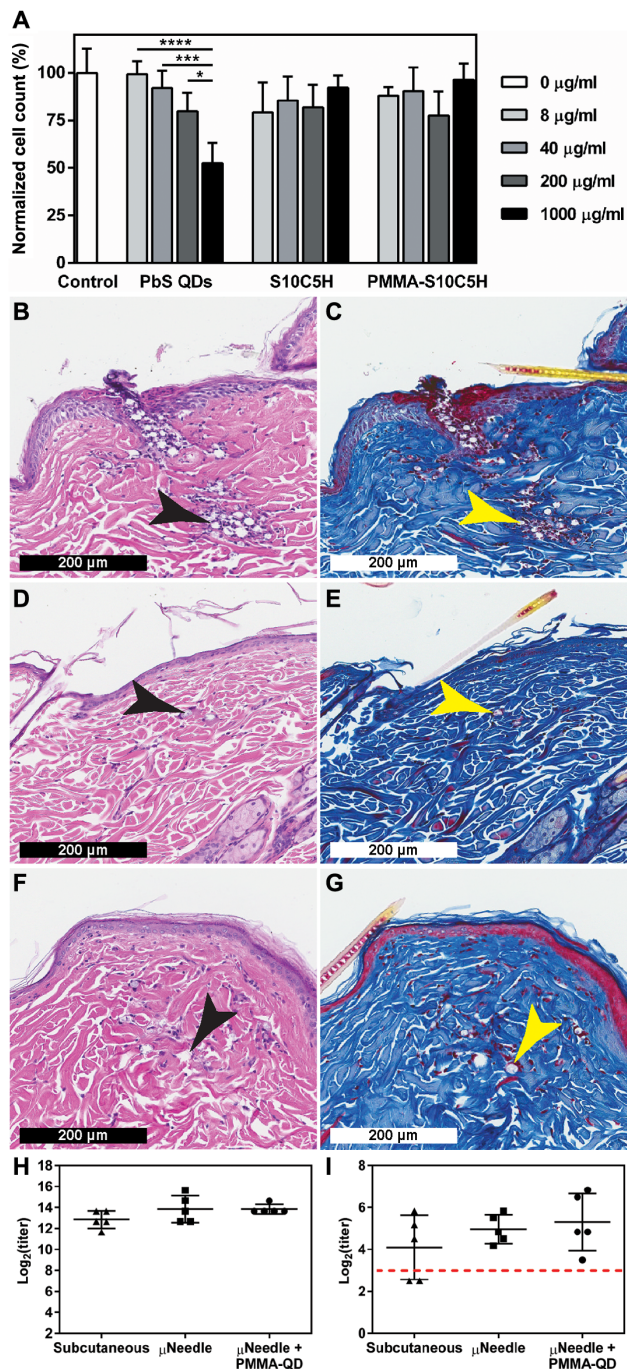


Fig. 7. Biological response to PMMA-encapsulated QDs. (A) *In vitro* cytotoxicity of commercially available PbS QDs compared to unencapsulated and PMMA-encapsulated S10C5H QDs over 24 hours in a mouse macrophage cell line (Raw 264.7). $n = 3$, $*P < 0.05$, $***P < 0.001$, and $****P < 0.0001$ (two-way ANOVA with Tukey's multiple comparisons). Representative histological samples collected from rats receiving microneedle-delivered PMMA particles containing S10C5H QDs (B and C) 1 day, (D and E) 2 weeks, and (F and G) 4 weeks after administration stained with hematoxylin and eosin or Masson's trichrome, respectively. Arrows indicate the location of microparticles. (H) Total anti-poliovirus type 2 immunoglobulin G antibody titers and (I) neutralizing poliovirus type 2 antibody titers showing no differences after three doses of IPV2 delivered via subcutaneous injections or microneedles with or without PMMA-encapsulated QDs, $n = 5$. Dashed line indicates the threshold above which humans are considered immune.

traditional needles, as has been shown elsewhere (34). Further, a previous study has shown that tip angle does not significantly affect pain upon needle insertion (35), so the effect of α (effective tip angle) on pain perception was not considered. These needles are slightly smaller in diameter than a 30-gauge needle and therefore should minimize both pain and the force required for skin penetration (36). Last, the lateral microneedle spacing results in a patch, and subsequently intradermal pattern, with a footprint of 0.25 cm^2 . This spacing was sufficiently large to allow each needle to act independently and thereby allow force requirements to scale linearly with needle number (37).

Over the past decade, smartphones have become ubiquitous in many areas of the world, including the developing world despite limited infrastructure (38). Because these phones offer on-board processing power, camera applications, and inexpensive consumer-grade camera modules, we chose to adapt an existing smartphone to enable NIR imaging rather than build a completely new imaging system. In addition, we believe that familiarity with the function of these devices will lessen the learning curve for NIR imaging in a field setting. Whereas a stock Nexus 5X camera is built with a short-pass filter to prevent NIR light from affecting images, we wanted the exact opposite—the elimination of light in the visible range and passage of NIR light. In addition, we needed the new filters to block reflected light from LED illumination. Therefore, after stripping the stock short-pass filter, we added a pair of 850-nm long-pass filters, which would block both environmental light and LED illumination. A dielectric filter was used to impose a sharp cutoff at 850 nm and paired with an 850-nm color glass filter to eliminate the passage of visible light entering the filter at very small angles, which we observed to be problematic with the dielectric filter alone (39). These optics were fit into a 3D-printed phone case customized for SM1-threaded components (1.035"-40) to fit with commercially available optical components.

Because both excitation and emission light can be absorbed by the body, we needed to create a system where both stages were within the optical imaging window. Although QDs are broadly excitable and exhibit higher quantum yield when excited at lower wavelengths (UV and visible light), high absorption from tissue components such as hemoglobin, water, and melanin at these wavelengths greatly attenuates the signal. Given previous studies examining the relative absorption of these components, excitation at higher wavelengths was deemed worth the trade-off. For example, our leading candidate, S10C5H, exhibited a PL QY of $43.6 \pm 0.1\%$ upon excitation with a 405-nm laser and a PL QY of $31.3 \pm 0.1\%$ when excited with an 808-nm laser, but would be subjected to an increase in absorption from hemoglobin and melanin on the order of one log unit each (40). We chose to use a 780-nm LED rather than a laser because of the reduced cost, safety concerns, and maintenance combined with improved portability. Adapting a laser to this setup would have required a diffusor or beam splitter to spread the light, safety mechanisms, and potentially some type of cooling apparatus. These components would add cost, complexity, and size, which are undesirable for distributed mobile use. Alternatively, an LED offered low cost, inherently diffuse illumination, and safety/power advantages. The only consideration necessary to use an LED was the considerably wider emission profile (28-nm full width at half maximum); however, this was solved using a simple 800-nm short-pass filter to ensure a 50-nm gap between excitation light and light collected by the adapted smartphone.

NIR images collected with the smartphone at various ISO and shutter speed ratings were manually cropped to enable the comparison of NIR signal intensity over time. Manual ISO and shutter speeds were necessary to enable longitudinal comparison. The auto-exposure setting was not well adapted for NIR imaging, as might be expected, and would often select higher exposure settings to make the field brighter to the point where the background was bright and the signal was highly saturated. Selection of the correct ISO for a pattern was critical for accurate analysis of both signal-to-noise ratio (SNR) as well as machine learning classification. To enable accurate SNR quantification, consistent imaging settings that produced nonsaturated pixels at all time points were selected. In the future, custom autoexposure settings could be implemented to automate this process.

The greatest reduction in user-identifiable signal occurred soon after administration, suggesting that some microneedles had not delivered QD-loaded microparticles to a sufficient depth—a phenomenon possibly exacerbated by the high elasticity of rodent skin (41). A portion of particles may have been deposited on the skin rather than in the skin and thereafter cleared by external perturbation. The QD signal stabilizes rather quickly and then presents a fairly consistent SNR at 3, 6, and 9 months, indicating that microparticle clearance likely primarily occurs at early time points (less than 3 months). This is further supported by the imaging of patterns in vivo at short time points, which showed considerable loss in the days after application before stabilizing.

AlexNet was chosen for its classification accuracy, having been originally trained on more than 1 million images and having demonstrated the ability to classify images into 1000 categories (20). Despite relatively little training data (30 images per pattern), AlexNet classified images with high accuracy. Overall, 80 images were tested for the circular pattern, 70 for the cross pattern, and 60 for the rectangular pattern originating from five distinct applications per pattern. The modified transfer-based convolutional neural network using AlexNet provided accurate detection confidence. Further, because there was no trend toward lower machine learning classification probability at 3, 6, and 9 months, it appears that the patterns are stable after an acute period of signal loss, which is also supported by short-term quantitative data and long-term qualitative data. On the basis of optical images of microneedles before and after administration, in vivo NIR imaging, and projections for photobleaching from in vitro experiment, we estimate that <1 µg of particles (<600 ng of QDs) is required to retain a detectable signal for 5 years.

Regarding accuracy, machine learning algorithms for image classification match and typically exceed manual inspection (42, 43). Whereas the human eye is ill equipped to distinguish low grayscale value differences in images that are dim or have poor contrast (for example, grayscale values of 1 versus 10), AlexNet's ability to use quantitative rather than qualitative information seems to make this distinction trivial. This effect is readily apparent when the grayscale photo values are represented as a rainbow heat map. AlexNet was particularly valuable when markings were missing, dim, or imaged at an unusual angle. Given the minimal training data used, it was important that images were collected using settings that roughly approximated the range of brightness/signal spread of images used for training. More training data and/or consistent autoexposure would mitigate this potential issue long term. Similarly, more patterns could be incorporated into the model to expand the variety of data that can be encoded. In the real-world use case, this automated classification

will eliminate classification subjectivity that could interfere with the accuracy of this approach. Synthetic data could also be produced using image augmentation to train the algorithm without the need for actual patch applications. However, the accuracy of this method could be lower if the variability in application exhibited in the synthetic data did not replicate the features of real microneedle patch applications in the test data. In our experience, training AlexNet with 5000 synthetic images yielded a real-world data classification accuracy of 92% for the circle and 97% for both the cross and the rectangle. Future training data could also include a fourth classification category for all images that do not closely resemble any of the patterns. This would be essential for real-world use when the presence of a pattern is uncertain.

For this encoding system to be clinically useful, microneedles and NIR microparticles must be biocompatible and, if applicable, maintain the utility of any codelivered vaccines. Histology showed that the particles were well tolerated in the body, similar to largely inert PMMA-based tattoo dyes (44), although some macrophages were observed. The accumulation of macrophages observed around the particles was less than other studies have shown for poly(lactic-co-glycolic acid) microparticles (45), for example, which are present in many U.S. Food and Drug Administration–approved drug delivery systems (46). In addition, histological images demonstrated that microneedle-delivered particles were delivered to a depth similar to professional tattoos (47), which supports their potential for long-term NIR detection.

In addition to the stand-alone value of an intradermal information encoding and detection platform, this system may offer greater advantages when codelivered with vaccines. By delivering both agents in the same microneedle patch, there is the potential to reduce production cost advantages and eliminate the possibility of misuse (such as applying the encoding patch without the vaccine). However, to function in combination with microneedle vaccines currently under development, PMMA-encapsulated NIR QDs must not interfere with the robust immune response generated by intradermal antigen delivery. To ensure sufficient QD delivery and vaccine stability after fabrication (a process that includes multiple days under high vacuum), the amount of sucrose in the microneedle formulation and application time were both increased. Despite these modifications, a decrease in vaccine stability (IPV2 D-to-C conversion) was still observed and a considerable microneedle volume was not transferred to the skin during application, which would be expected to reduce the magnitude of the immune response. Nevertheless, microneedle-treated groups yielded total and neutralizing antibody titers against IPV2 that were similar with theoretical dose-matched subcutaneous injections and were above the threshold known to confer protection in humans, regardless of the presence of encapsulated QDs. This was observed despite substantial losses during formulation and administration and is likely due to the dose-sparing effects of intradermal delivery (16,17). Although the addition of polymer could have had an adjuvant effect, this was not observed, likely because of the well-tolerated, largely inert nature of our PMMA microparticles, as demonstrated in our histological data. These results support the clinical potential for using these microneedles to coadminister an invisible marking agent and a vaccine in one application.

This study provides support for long-lived, reliable pattern detection using QDs; however, like many preclinical studies, it is limited in duration and relies on small animal models. We present data

characterizing signal expression over 9 months in animals and in vitro accelerated solar light photobleaching, which suggest that detectable markings would persist to the target time point of 5 years. On the basis of histology and longitudinal imaging studies, we would not anticipate a substantial decrease in signal within 5 years after application; however, we did not explicitly demonstrate this because of time constraints, which exceed the typical life span of our animal model.

In summary, we have demonstrated proof of concept for a platform capable of invisibly recording data in the skin. To establish this system, we synthesized, encapsulated, and delivered cadmium-free and lead-free photostable QDs into the skin using a custom microneedle array, adapted a smartphone to create an inexpensive NIR imaging system, and demonstrated the ability to accurately detect patterns in vivo for a period of 9 months using a semiautomated machine learning algorithm. Transferring this technology to the clinic will require several additional steps including preclinical safety and toxicology studies, manufacturing scale-up, and first-in-human studies. Additional in vivo small animal studies will aid in the robust characterization of local and systemic responses to QD-loaded PMMA microparticles and microneedle patches to ensure quality, safety, and reliability. Formative studies in which users test the devices, including the packaging and labeling, will need to be conducted to improve components for commercialization and to manufacture devices for testing in human studies. Ultimately, we believe that this invisible, “on-body” technology opens up new avenues for decentralized data storage and biosensing applications that could influence the way medical care is provided, especially in the developing world.

MATERIALS AND METHODS

Study design

These studies were designed to evaluate the suitability of intradermal NIR fluorescent microparticles as a reliable, long-term detection method. To evaluate this technology under typical field conditions, we used an adapted smartphone in ambient light to determine success criteria, except in circumstances where spectral and/or highly quantitative data were necessary to characterize our materials. In vivo studies were generally preferred to assess the performance of our delivery and detection systems and animals were randomly assigned to different experimental groups at the onset of each study. The use of machine learning for detection eliminated the need for blinding. In vitro studies were performed with three replicates and in vivo studies with five replicates, unless otherwise noted. Individual subject-level data are reported in data file S1.

QD synthesis

Stoichiometric CuInSe₂ cores were synthesized by mixing 1.5 mmol of copper(I) iodide and 1.5 mmol of indium(III) acetate in 1.5 ml of 1-dodecanethiol (DDT) and 45 ml of 1-octadecene (ODE) based on a modified procedure (48). The reaction mixture was then degassed under vacuum for 20 min, purged with nitrogen for 20 min, and degassed for an additional 45 min at 120°C. Next, 1.5 ml of oleic acid was added into the mixture, and the solution was degassed for 20 min. After another 20-min nitrogen purge, the solution was heated to 175°C before the injection of selenium stock solution. A selenium stock solution was first prepared by mixing 3 mmol of selenium powder and 3 ml of oleylamine (OLA) in 3 ml of DDT

(49). The selenium solution was degassed under vacuum for at least 30 min at 60°C before injected into the reaction mixture. The reaction mixture was heated to 200°C and maintained at this temperature for 30 min under the protection of nitrogen.

ZnS:Al shells were formed around CuInSe₂ cores through the dropwise addition of a stock solution containing zinc and aluminum. The zinc precursor of the stock solution was prepared by mixing 30 mmol of zinc acetate in 30 ml of OLA and 30 ml of ODE, degassing for 20 min, and purging with nitrogen for 20 min. Next, the solution was heated to 120°C and degassed under vacuum. The Al precursor mixture consisting of 9 mmol of Al(IPA)₃, 5.4 ml of DDT, and 36 ml of ODE was degassed for 20 min and purged with nitrogen for 20 min. The vessel was then sealed and sonicated for 1 hour at 60°C (50). The aluminum stock solution was then added to the zinc stock solution using a glass syringe and long needle. After mixing the zinc and aluminum precursors, the resulting shell stock solution was added dropwise to the reaction mixture of CuInSe₂ cores at 0.1 ml/min using a pump. At the same time, 15 ml of DDT was added at a rate of 0.5 ml/min to thermally trigger the release of sulfur (51). The reaction was allowed to proceed for varying amounts of time, depending on the formulation. Afterward, the reaction solution was cooled to room temperature and precipitated twice into acetone, once into a 50:50 solution of acetone and methanol, and twice more into methanol. Between each round of precipitation, QDs were resuspended in a minimal amount of toluene and oleic acid that was added dropwise until the solution turned transparent. After the final precipitation step, QDs were dispersed in toluene.

Photobleaching analysis

Organic dyes required different imaging conditions than inorganic dyes and QDs because of their small Stokes shift and therefore high propensity to self-quench in the dry state. Organic fluorophores were dissolved in water at a concentration of 10 µg/ml, which was found to be within the linear absorbance range for all dyes. Fifty microliters of each dye was added to a black-walled 384-well plate, covered with a 1-mm-thick quartz slide, and sealed with parafilm at the edges to prevent evaporation during light exposure. The plate was then read using a Tecan Infinite M200 Spectrophotometer to determine the fluorescence intensities of Alexa Fluor 790 [784/814-nm excitation/emission (ex/em)], DyLight 800 (760/810-nm ex/em), IRDye 800CW (768/798-nm ex/em), IR-820 (710/820-nm ex/em), Sulfo-Cyanine7 (750/773-nm ex/em), VivoTag 800 (785/815-nm ex/em), and indocyanine green (805/835-nm ex/em).

Samples were then placed under a 300W PV Cell Testing Solar Simulator Model 16S-300-002 (Solar Light). The ozone-free short-arc xenon lamp was used with an air mass 1.5 filter and focusing lens to expose samples to conditions mimicking the spectral distribution and power density of sunlight at sevenfold the intensity of the sun (695 mW/cm²). A 2-mm-thick piece of pigmented human cadaver skin from donors age 21 to 68 years who self-identified as African American was overlaid onto the sample to recapitulate light absorption by tissue above an intradermal fluorophore. Skin was kept hydrated by a continuous flow of water over the surface and chilled from below using a CP-200HT-TT Peltier-Thermoelectric Cold Plate Cooler (TE Technology) to prevent damage to the skin. Samples were periodically removed from the solar simulator and imaged using the spectrophotometer. This experiment was repeated three times with one replicate each.

Inorganic dyes and QDs were capable of being imaged in their dry state, so a modified protocol was used. Holes were punched in a black silicone sheet using a 2-mm stainless steel biopsy punch to create space for dyes. The silicone sheet was then treated with air plasma for 1 min on high power at 500 mtorr. The sheet was then placed on a 2.54 cm by 2.54 cm quartz slide, which allowed it to adhere in a water-tight manner. Suspensions of Infrared Down-Conversion 2 (IRDC2) and IRDC3 at 10 mg/ml in water were deposited 2 μ l at a time and allowed to dry until a total of 10 μ l had been deposited. The same steps were performed for ZnS:Al-coated CuInSe₂ QD solutions at 10 mg/ml in toluene. Double-sided tape and parafilm were then used to seal a glass slide to the other side of the black silicone. The sample was then placed quartz slide-up beneath a piece of pigmented cadaveric skin in a metal block under continuous hydration on a cold plate cooler and exposed to light at sevenfold solar intensity. At predetermined time points, samples were removed from light and imaged using a custom NIR-imaging platform consisting of a 500-mW laser emitting at 808 nm and thermoelectric-cooled mount powered by a LDC210C Laser Diode Controller and TED200C Temperature Controller, a 15 \times achromatic Galilean beam expander, protected silver mirror, 850-nm color glass long-pass emission filter, and a high-sensitivity USB 3.0 complementary metal-oxide semiconductor camera (DCC3240N) affixed to an optical breadboard (Thor Labs) inside a dark work enclosure (U.S. Laser). Images were collected at different exposure lengths for different dyes ranging from 10 to 2000 ms. The longest exposure length that did not saturate the 10-bit pixel depth was used for each dye at all time points. Owing to the length of this experiment, all samples ($n = 3$) were run simultaneously. For all photobleaching experiments, skin was replaced every 2 to 4 days to reduce the effects of melanin degradation. Intensity data were quantified using ImageJ (National Institutes of Health) and normalized by selecting a region of interest (ROI) around a well and comparing the intensity above background in that image to the intensity above background of the corresponding ROI at the beginning of the experiment (52). All photobleaching data are reported as simulated days of exposure based on a 12-hour light/dark cycle.

QD encapsulation

QD-loaded PMMA microparticles were formed using an oil-in-water emulsion/solvent evaporation technique. Briefly, 150 mg of QDs and 100 mg of PMMA were dissolved in 2 ml of dichloromethane. This solution was then added to 50 ml of 1% poly(vinyl alcohol) (PVA) [88% hydrolyzed, M_w (weight-average molecular weight), 31,000] solution in water. The resulting solution was emulsified at 5000 revolutions per minute (RPM) for 1 min using a T 18 digital ULTRA-TURRAX homogenizer (IKA Works) and subsequently stirred at 250 RPM for 3 hours to allow solvent to evaporate. Particles were centrifuged at 1000 relative centrifugal force (RCF) after which the supernatant was removed. Particles were then washed four times by adding deionized water, centrifugation at 1000 RCF, and supernatant removal. The resulting particles were resuspended in deionized water and measured using a Multisizer 3 (Beckman Coulter) with a 100- μ m aperture. Data were smoothed using an 11-frame moving window and plotted as a histogram with 300 equal-sized bins ranging from 2.1 to 59.9 μ m. QD-loaded microparticles were then imaged using optical microscopy and scanning electron microscopy (SEM) to observe their shape. Optical imaging was performed using an Olympus MX40 inspection microscope with a TouPCam industrial digital camera (TouPCam Photonics). In preparation for SEM, samples were deposited on

double-sided carbon tape and coated with a thin layer of Au/Pd using a Hummer 6.2 Sputtering System (Anatech) to prevent charging. Imaging was then performed using a JEOL JSM-5600LV scanning electron microscope with an acceleration voltage of 5 kV.

The pH stability of S10C5H QDs in PMMA was determined by casting a solution onto the bottom of a plate to prevent agitation upon addition of the buffer. QDs (150 mg) and 100 mg of PMMA were added to 2 ml of dichloromethane and sonicated for 5 min. Using a glass pipette, about 5 μ l of the QD solution was added to the bottom of a 96-well black-walled glass-bottom plate and dried overnight. PBS (200 μ l) was then added to each well, and the samples were incubated at 37°C for 24 hours. At this stage, the initial intensity of the QD-PMMA samples were analyzed using a custom NIR-imaging platform as described above. To investigate the effect of pH on the intensity of the QDs, the PBS was replaced by a buffer solution at pH 4, 5, 6, 7.4 (PBS), or 10. The plate was then sealed to minimize solvent loss and incubated at 37°C. After 1, 4, and 22 hours, samples were removed from the incubator, and QD intensity was measured using the custom NIR-imaging system with a 40-ms collection time. Intensity data were quantified in ImageJ and normalized by selecting an ROI around a well and comparing the intensity above background in that image to the intensity above background of the corresponding ROI at the beginning of the experiment.

Dissolvable microneedle fabrication and characterization

Water-soluble microneedle patches containing QD-loaded microparticles at the needle tips were fabricated using a solvent casting process. First, microparticles were resuspended in water, pipetted onto the top of the PDMS mold (4 μ l per microneedle), and centrifuged at 3234 RCF for 5 min. Excess solution was cleared from the top of the mold, and the solution was allowed to dry leaving behind particles in the tips of the mold. This process was repeated when loading was lower than desired or unevenly distributed. About 300 μ l of a 17% (w/v) sucrose and 17% (w/v) PVA solution in water was then dispensed on top of the mold and centrifuged at 3234 RCF for 5 min. Molds were then left at room temperature overnight in a laminar flow hood as an initial drying stage. Laser-cut acrylic discs were then affixed to double-sided tape and attached to the back side of the solidified microneedle patch. The patch was then carefully removed from the mold and stored for an additional 72 hours under vacuum desiccation.

Smartphone modifications

A smartphone camera was adapted with commercially available optical components purchased from Thorlabs to enhance NIR QD detection in the NIR. To enable NIR detection, the stock short-pass IR filter was removed from a Google Nexus 5X smartphone. A smartphone case was then designed and 3D-printed to interface tightly with optical components having SM1 threading directly in front of the rear-facing camera. An 850-nm long-pass dielectric filter (FEL0850) and 850-nm long-pass color glass filter (FGL850) were placed in parallel in a lens tube attached to the smartphone case and held in place with a retaining ring. For QD illumination, a 780-nm, 200-mW mounted LED (M780L3) powered by a T-Cube LED Driver (LEDD1B) and 15-V, 2.4-A power supply (KPS101) was used. To augment the shape and spectrum of emission, an 800-nm dielectric short-pass filter (FEL0800) and aspheric condenser lens with diffuser (ACL2520U-DG6-B) were used in an adjustable lens tube. All imaging was performed using the Camera FV-5 Lite app (FGAE Studios).

Biocompatibility of encapsulated QDs

Microneedles containing encapsulated QDs were administered to Wistar rats (Charles River Laboratories) 8 to 12 weeks of age weighing about 250 g to assess *in vivo* biocompatibility. Rats were anesthetized via continuous inhalation of 2.5% isoflurane throughout the administration and imaging process. Hair removal was performed before microneedle administration by shaving the rear flank with an electric razor and applying depilatory cream for about 2 min. The area was then rinsed to remove excess hair, sterilized using an ethanol swab, and allowed to dry. Microneedles were applied using an MPatch Mini spring-loaded applicator (Micropoint Technologies) for 2 min. Rats were returned to their cages and housed until terminal time points at 1 day, 2 weeks, and 4 weeks ($n = 4$ per time point). At the time of sacrifice, rats were euthanized via CO₂ asphyxiation. Skin was explanted and fixed in formalin-free tissue fixative (Sigma-Aldrich) for 24 to 72 hours. The relevant portion of the tissue was identified using the adapted smartphone, transferred to 70% ethanol, and embedded in paraffin wax. Samples were sectioned and stained with hematoxylin and eosin or Masson's trichrome. Interpretation of the foreign body reaction was performed under the guidance of an experienced veterinary pathologist.

Longitudinal *in vivo* imaging of NIR patterns

Two longitudinal imaging experiments were performed to assess the short-term loss of signal after administration and long-term residence of microneedle-delivered particles. In both cases, QDs were administered to rats using dissolvable microneedle patches as described above and imaged periodically to observe signal intensity over time. At each time point, rats were anesthetized under continuous inhalation of 2.5% isoflurane and imaged with the 780-nm LED and NIR-adapted smartphone, maintaining a consistent imaging distance.

In the first experiment, microneedles containing PMMA-encapsulated and free (unencapsulated) ZnS:Al-coated CuInSe₂ QDs were compared to evaluate the potential benefits of encapsulation on initial signal intensity and signal retention. Encapsulated QDs were embedded in dissolvable microneedles using the protocol detailed above. Unencapsulated QDs were not readily dispersible in water, so the loading procedure was slightly modified. Before loading, PDMS molds were treated with air plasma using a Harrick Plasma Cleaner PDC-091-HP on high power at 500 mtorr for 1 min. QDs in toluene (4 μ l per microneedle) were then deposited into the microneedle molds and centrifuged at 3234 RCF for 5 min. Toluene was then allowed to dry. A solution of sucrose and PVA was then applied to the molds and centrifuged into the needles and allowed to dry using the fabrication steps outlined above.

After applying 16-microneedle patches, the highest nonsaturating imaging settings were identified and used at all subsequent time points for that group. For the unencapsulated group, these settings were ISO 100 with a shutter speed of $1/30$ s. For the encapsulated group, these settings were ISO 100 with a shutter speed of $1/30$ or $1/200$ s. For each animal and time point, about 20 images were collected with slightly different aim of the LED, which was controlled independently from the camera that remained in a fixed location. An ImageJ macro was then used to split images into their three constituent red, green, and blue channels, save the red channel in grayscale format, and identify the images with the maximum intensity. This image with the best aim was then used for subsequent quantification of signal-above background. Briefly, 80-pixel circular ROIs were applied to each of the 16 dots in the 4×4 array to quantify the

average signal. The average grayscale intensity of the remaining pixels was subtracted to generate longitudinally comparable values for signal above background.

On the basis of this short-term study, a second long-term study was performed using encapsulated QDs in eight-needle microneedle patterns (circle, cross, or rectangle) for image detection and machine learning analysis. Arrays were administered at 0 (circle), 4 (cross), and 8 (rectangle) weeks to mimic a common vaccination schedule in the developing world. A separate group was started in parallel to generate an image dataset for training the machine learning algorithm. Images were collected every 2 weeks at a variety of ISO and shutter speeds, processed, and used for both SNR analysis and machine learning classification.

Microneedle-based vaccine delivery

The solution used to cast microneedles was altered in favor of additional sucrose (2:1 w/w sucrose:PVA) to potentially improve vaccine stability during processing. A solution of 34% (w/v) sucrose and 17% (w/v) PVA solution containing 3.2 DU of Salk IPV2 (MEF-1 strain; Statens Serum Institut) was centrifuged into PDMS microneedle molds using the procedures detailed above. After processing, some microneedle patches were collected, resuspended in assay buffer, and evaluated using a D-antigen-specific monoclonal sandwich enzyme-linked immunosorbent assay (ELISA) for IPV2 to determine the amount of the vaccine still in its immunity-conferring state. A monoclonal antibody against IPV2 poliovirus (HYB 294-06-02, Thermo Fisher Scientific) was used as both the capture and detection antibody, which was made possible because of the multiple identical binding sites on IPV. To avoid species cross-reactivity, a Lightning-Link Horseradish Peroxidase Kit (Novus Biologicals) was used to prebind the detection epitope. Briefly, 100 μ l of antibody diluted 1:1500 in carbonate buffer (pH 9.6) was added to each well of a Nunc Maxisorp LockWell 96-well plate and incubated overnight at 4°C on an orbital shaker. Plates were then washed with PBS containing 0.05% Tween 20 three times and incubated in 300 μ l of blocking buffer containing the wash buffer and 5% (w/v) nonfat milk for 1 hour at 37°C. Plates were again washed and then loaded with 50 μ l of samples. After 2 hours of incubation at 37°C, plates were washed five times and the Lightning Link-modified antibody was added at 1:833 in PBS. After 1-hour incubation, plates were washed another five times and then 100 μ l of a SIGMAFAST OPD substrate (Sigma-Aldrich) was added after resuspension according to the manufacturer's protocol. After a color change, 150 μ l of 1 M sulfuric acid was added to each well to stop the reaction, and absorbance values were read at 490 nm with a background reference of 630 nm using a spectrophotometer.

Microneedle patches not used for ELISA were applied to rats for a duration of 5 min using the protocol described above. After application, the portion of the microneedles remaining on the patch was collected, resuspended in assay buffer, and measured via the IPV2 D-antigen ELISA. A control group of rats received a dose-matched subcutaneous injection in the rear flank. These procedures were repeated 4 and 8 weeks later to provide rats with second and third doses. Rats were bled vial tail vein every 2 weeks after administration to collect serum for immunological analysis. Blood was collected in BD SST tubes (product no. 365967, Becton Dickinson) and used according to the manufacturer's protocol to obtain serum, which was subsequently stored at -20°C until use. A total anti-IPV2 antibody ELISA was performed in house using an indirect ELISA, as

previously described (53). IPV2 neutralizing antibody titers were determined by the U.S. Centers for Disease Control and Prevention using a protocol previously published (21).

Statistical analysis

Statistics were performed in GraphPad Prism using Student's *t* test for pairwise comparisons and one-way analysis of variance (ANOVA) with Tukey's multiple comparisons test for comparing multiple groups at a significance level of $\alpha = 0.05$. In vitro toxicity experiments evaluating both QD type and concentration were analyzed using two-way ANOVA at a significance level of $\alpha = 0.05$. All in vitro experiments were performed in experimental triplicate unless otherwise noted. All in vivo experiments were performed with five experimental replicates unless otherwise noted. Data are reported in the text as means \pm SD.

SUPPLEMENTARY MATERIALS

stm.sciencemag.org/cgi/content/full/11/523/eaay7162/DC1

Materials and Methods

Fig. S1. Optical properties of organic dyes.

Fig. S2. Evolution of fluorescence emission properties with shelling time.

Fig. S3. Fluorescence lifetime characterization of the S10C QD series.

Fig. S4. Composition and physical properties of S10C5H QDs.

Fig. S5. pH stability of PMMA-encapsulated QDs.

Fig. S6. Finite element analysis of mechanical forces on microneedles.

Fig. S7. Optimization of microneedle geometry using finite element analysis.

Fig. S8. Machine learning training and validation.

Table S1. Spectral characterization of custom QD formulations.

Table S2. Multiexponential fitting parameters for photoluminescence decay curves.

Movie S1. Intradermal administration and imaging of encapsulated QDs.

Data file S1. Individual subject-level data.

References (54–62)

[View/request a protocol for this paper from Bio-protocol.](#)

REFERENCES AND NOTES

- Legesse, W. Dechasa, An assessment of child immunization coverage and its determinants in Sinana District, Southeast Ethiopia. *BMC Pediatr.* **15**, 31 (2015).
- R. E. Black, S. Cousens, H. L. Johnson, J. E. Lawn, I. Rudan, D. G. Bassani, P. Jha, H. Campbell, C. F. Walker, R. Cibulskis, T. Eisele, L. Liu, C. Mathers; Child Health Epidemiology Reference Group of WHO and UNICEF, Global, regional, and national causes of child mortality in 2008: A systematic analysis. *Lancet* **375**, 1969–1987 (2010).
- P. G. Szilagyi, L. E. Rodewald, Missed opportunities for immunizations: A review of the evidence. *J. Public Health Manag. Pract.* **2**, 18–25 (1996).
- C. M. Pirkle, A. Dumont, M. V. Zunzunegui, Medical recordkeeping, essential but overlooked aspect of quality of care in resource-limited settings. *Int. J. Qual. Health Care* **24**, 564–567 (2012).
- V. S. Fields, H. Safi, C. Waters, J. Dillaha, L. Capelle, S. Riklon, J. G. Wheeler, D. T. Haselow, Mumps in a highly vaccinated Marshallese community in Arkansas, USA: An outbreak report. *Lancet Infect. Dis.* **19**, 185–192 (2019).
- D. W. Westphal, A. Eastwood, A. Levy, J. Davies, C. Huppatz, M. Gilles, H. Lyttle, S. A. Williams, G. K. Dowse, A protracted mumps outbreak in Western Australia despite high vaccine coverage: A population-based surveillance study. *Lancet Infect. Dis.* **19**, 177–184 (2019).
- A. Lo Vecchio, M. D. Cambriglia, M. C. Fedele, F. W. Basile, F. Chiatto, M. Miraglia del Giudice, A. Guarino, Determinants of low measles vaccination coverage in children living in an endemic area. *Eur. J. Pediatr.* **178**, 243–251 (2019).
- M. Miles, T. K. Ryman, V. Dietz, E. Zell, E. T. Luman, Validity of vaccination cards and parental recall to estimate vaccination coverage: A systematic review of the literature. *Vaccine* **31**, 1560–1568 (2013).
- W. Tao, M. Petzold, B. C. Forsberg, Routine vaccination coverage in low- and middle-income countries: Further arguments for accelerating support to child vaccination services. *Glob. Health Action* **6**, 20343 (2013).
- J. J. Valadez, L. H. Weld, Maternal recall error of child vaccination status in a developing nation. *Am. J. Public Health* **82**, 120–122 (1992).
- I. U. Ogbuanu, A. J. Li, B. M. Anya, M. Tamadji, G. Chirwa, K. W. Chiwaya, M. E. Djalal, D. Cheikh, Z. Machekanyanga, J. Okeibunor, C. Sanderson, R. Mihigo, Can vaccination coverage be improved by reducing missed opportunities for vaccination? Findings from assessments in Chad and Malawi using the new WHO methodology. *PLOS ONE* **14**, e0210648 (2019).
- A. Katib, D. Rao, P. Rao, K. Williams, J. Grant, A prototype of a novel cell phone application for tracking the vaccination coverage of children in rural communities. *Comput. Methods Programs Biomed.* **122**, 215–228 (2015).
- A. K. Jain, S. S. Arora, L. Best-Rowden, K. Cao, P. S. Sudhish, A. Bhatnagar, Y. Koda, Giving infants an identity: Fingerprint sensing and recognition, in *Proceedings of the Eighth International Conference on Information and Communication Technologies and Development (ICTD 2016)*, Ann Arbor, MI, USA, 03 to 06 June, 2016 (ACM, 2016).
- R. Nagar, P. Venkat, L. D. Stone, K. A. Engel, P. Sudda, M. Shah Nawaz, A cluster randomized trial to determine the effectiveness of a novel, digital pendant and voice reminder platform on increasing infant immunization adherence in rural Udaipur, India. *Vaccine* **36**, 6567–6577 (2018).
- N. G. Roupheal, M. Paine, R. Mosley, S. Henry, D. V. McAllister, H. Kalluri, W. Pewin, P. M. Frew, T. Yu, N. J. Thornburg, S. Kabbani, L. Lai, E. V. Vassilieva, I. Skountzou, R. W. Compans, M. J. Mulligan, M. R. Prausnitz; TIV-MNP 2015 Study Group, The safety, immunogenicity, and acceptability of inactivated influenza vaccine delivered by microneedle patch (TIV-MNP 2015): A randomised, partly blinded, placebo-controlled, phase 1 trial. *Lancet* **390**, 649–658 (2017).
- M. R. Prausnitz, Engineering microneedle patches for vaccination and drug delivery to skin. *Annu. Rev. Chem. Biomol.* **8**, 177–200 (2017).
- Y. He, C. Hong, J. Li, M. T. Howard, Y. Li, M. E. Turvey, D. S. S. M. Uppu, J. R. Martin, K. Zhang, D. J. Irvine, P. T. Hammond, Synthetic charge-invertible polymer for rapid and complete implantation of layer-by-layer microneedle drug films for enhanced transdermal vaccination. *ACS Nano* **12**, 10272–10280 (2018).
- E. V. Vassilieva, H. Kalluri, D. McAllister, M. T. Taheribhai, E. S. Esser, W. P. Pewin, J. A. Pulit-Penalosa, M. R. Prausnitz, R. W. Compans, I. Skountzou, Improved immunogenicity of individual influenza vaccine components delivered with a novel dissolving microneedle patch stable at room temperature. *Drug Deliv. Transl. Res.* **5**, 360–371 (2015).
- D. Zehrunge, C. Jarrhian, B. Giersing, D. Kristensen, Exploring new packaging and delivery options for the immunization supply chain. *Vaccine* **35**, 2265–2271 (2017).
- A. Krizhevsky, I. Sutskever, G. E. Hinton, ImageNet classification with deep convolutional neural networks. *Commun. ACM* **60**, 84–90 (2017).
- W. C. Weldon, M. S. Oberste, M. A. Pallansch, Standardized methods for detection of poliovirus antibodies. *Methods Mol. Biol.* **1387**, 145–176 (2016).
- K. T. Rim, K. H. Koo, J. S. Park, Toxicological evaluations of rare earths and their health impacts to workers: A literature review. *Saf. Health Work* **4**, 12–26 (2013).
- K. J. McHugh, L. Jing, A. M. Behrens, S. Jayawardena, W. Tang, M. Gao, R. Langer, A. Jaklenec, Biocompatible semiconductor quantum dots as cancer imaging agents. *Adv. Mater.* **30**, e1706356 (2018).
- M. R. Hamblin, T. N. Demidova, Mechanisms of low level light therapy. *Proc. SPIE* **6140**, (2006).
- A. M. Smith, M. C. Mancini, S. M. Nie, Bioimaging: Second window for in vivo imaging. *Nat. Nanotechnol.* **4**, 710–711 (2009).
- A. L. Antaris, H. Chen, K. Cheng, Y. Sun, G. Hong, C. Qu, S. Diao, Z. Deng, X. Hu, B. Zhang, X. Zhang, O. K. Yaghi, Z. R. Alamparabail, X. Hong, Z. Cheng, H. Dai, A small-molecule dye for NIR-II imaging. *Nat. Mater.* **15**, 235–242 (2016).
- H. R. Wilson, P. K. Nadeau, B. F. Jaworski, J. B. Tromberg, A. J. Durkin, Review of short-wave infrared spectroscopy and imaging methods for biological tissue characterization. *J. Biomed. Opt.* **20**, 030901 (2015).
- A. Baranska, A. Shawket, M. Jouve, M. Baratin, C. Malosse, O. Voluzan, T.-P. Vu Manh, F. Fiore, M. Bajénoff, P. Benaroch, M. Dalod, M. Malissen, S. Henri, B. Malissen, Unveiling skin macrophage dynamics explains both tattoo persistence and strenuous removal. *J. Exp. Med.* **215**, 1115–1133 (2018).
- K. Matsuo, Y. Yokota, Y. Zhai, Y.-S. Quan, F. Kamiyama, Y. Mukai, N. Okada, S. Nakagawa, A low-invasive and effective transcutaneous immunization system using a novel dissolving microneedle array for soluble and particulate antigens. *J. Control. Release* **161**, 10–17 (2012).
- E. Z. Loizidou, N. A. Williams, D. A. Barrow, M. J. Eaton, J. McCrory, S. L. Evans, C. J. Allender, Structural characterisation and transdermal delivery studies on sugar microneedles: Experimental and finite element modelling analyses. *Eur. J. Pharm. Biopharm.* **89**, 224–231 (2015).
- M. Alam, A. Geisler, D. Sadhwani, A. Goyal, E. Poon, M. Nodzinski, M. R. Schaeffer, R. Tung, K. Minkis, Effect of needle size on pain perception in patients treated with botulinum toxin Type A injections: A randomized clinical trial. *JAMA Dermatol.* **151**, 1194–1199 (2015).
- H. S. Gill, M. R. Prausnitz, Does needle size matter? *J. Diabetes Sci. Technol.* **1**, 725–729 (2007).
- L. Arendt-Nielsen, H. Egekvist, P. Bjerring, Pain following controlled cutaneous insertion of needles with different diameters. *Somatosen. Mot. Res.* **23**, 37–43 (2006).
- H. S. Gill, D. D. Denson, B. A. Burris, M. R. Prausnitz, Effect of microneedle design on pain in human subjects. *Clin. J. Pain* **24**, 585–594 (2010).

35. K. A. Præstmark, M. L. Jensen, N. B. Madsen, J. Kildegaard, B. M. Stallknecht, Pen needle design influences ease of insertion, pain, and skin trauma in subjects with type 2 diabetes. *BMJ Open Diabetes Res. Care* **4**, e000266 (2016).
36. M. L. Masid, R. H. Ocaña, M. J. Gil, M. C. Ramos, M. E. Roig, M. R. Carreño, J. C. Morales, M. L. Carrasco, L. M. Hidalgo, A. M. Felices, A. H. Castaño, P. C. Romero, P. F. Martínez, R. Sánchez-De la Rosa, A patient care program for adjusting the autoinjector needle depth according to subcutaneous tissue thickness in patients with multiple sclerosis receiving subcutaneous injections of glatiramer acetate. *J. Neurosci. Nurs.* **47**, E22–E30 (2015).
37. O. Olatunji, D. B. Das, M. J. Garland, L. Belaid, R. F. Donnelly, Influence of array interspacing on the force required for successful microneedle skin penetration: Theoretical and practical approaches. *J. Pharm. Sci.* **102**, 1209–1221 (2013).
38. S. K. Vashist, E. M. Schneider, J. H. Luong, Commercial smartphone-based devices and smart applications for personalized healthcare monitoring and management. *Diagnostics* **4**, 104–128 (2014).
39. R. M. Lerner, Limitations in the use of dielectric interference filters in wide angle optical receivers. *Appl. Optics* **10**, 1914–1918 (1971).
40. H. Chung, T. Dai, S. K. Sharma, Y.-Y. Huang, J. D. Carroll, M. R. Hamblin, The nuts and bolts of low-level laser (light) therapy. *Ann. Biomed. Eng.* **40**, 516–533 (2012).
41. J. C. J. Wei, G. A. Edwards, D. J. Martin, H. Huang, M. L. Crichton, M. A. F. Kendall, Allometric scaling of skin thickness, elasticity, viscoelasticity to mass for micro-medical device translation: From mice, rats, rabbits, pigs to humans. *Sci. Rep.* **7**, 15885 (2017).
42. K. He, X. Zhang, S. Ren, J. Sun, Deep Residual Learning for Image Recognition, in *Proceedings of IEEE Conference on Computer Vision Pattern Recognition (IEEE, 2016)*, pp. 770–778.
43. O. Russakovsky, J. Deng, H. Su, J. Krause, S. Satheesh, S. Ma, Z. Huang, A. Karpathy, A. Khosla, M. Bernstein, A. C. Berg, L. Fei-Fei, ImageNet large scale visual recognition challenge. *Int. J. Comput. Vis.* **115**, 211–252 (2015).
44. J.-s. Choi, Y. Zhu, H. Li, P. Peyda, T. T. Nguyen, M. Y. Shen, Y. M. Yang, J. Zhu, M. Liu, M. M. Lee, S.-S. Sun, Y. Yang, H.-h. Yu, K. Chen, G. S. Chuang, H.-R. Tseng, Cross-linked fluorescent supramolecular nanoparticles as finite tattoo pigments with controllable intradermal retention times. *ACS Nano* **11**, 153–162 (2017).
45. J. M. Anderson, M. S. Shive, Biodegradation and biocompatibility of PLA and PLGA microspheres. *Adv. Drug Deliver. Rev.* **28**, 5–24 (1997).
46. H. Zhong, G. Chan, Y. Hu, H. Hu, D. Ouyang, A comprehensive map of FDA-approved pharmaceutical products. *Pharmaceutics* **10**, 263 (2018).
47. K. Sardana, R. Ranjan, S. Ghunawat, Optimising laser tattoo removal. *J. Cutan. Aesthet. Surg.* **8**, 16–24 (2015).
48. H. Z. Zhong, Z. B. Wang, E. Bovero, Z. H. Lu, F. C. J. M. van Veggel, G. D. Scholes, Colloidal CuInSe_2 nanocrystals in the quantum confinement regime: Synthesis, optical properties, and electroluminescence. *J. Phys. Chem. C* **115**, 12396–12402 (2011).
49. Y. Liu, D. Yao, L. Shen, H. Zhang, X. Zhang, B. Yang, Alkylthiol-enabled Se powder dissolution in oleylamine at room temperature for the phosphine-free synthesis of copper-based quaternary selenide nanocrystals. *J. Am. Chem. Soc.* **134**, 7207–7210 (2012).
50. Z. Li, W. Yao, L. Kong, Y. Zhao, L. Li, General method for the synthesis of ultrastable core/shell quantum dots by aluminum doping. *J. Am. Chem. Soc.* **137**, 12430–12433 (2015).
51. K. Ding, L. H. Jing, C. Y. Liu, Y. Hou, M. Y. Gao, Magnetically engineered Cd-free quantum dots as dual-modality probes for fluorescence/magnetic resonance imaging of tumors. *Biomaterials* **35**, 1608–1617 (2014).
52. C. A. Schneider, W. S. Rasband, K. W. Eliceiri, NIH Image to ImageJ: 25 years of image analysis. *Nat. Methods* **9**, 671–675 (2012).
53. R. Mishra, T. K. Bhattacharyya, T. K. Maiti, Theoretical analysis and simulation of SU-8 microneedles for effective skin penetration and drug delivery, in *2015 IEEE Sensors (IEEE, 2015)*, pp. 1769–1772.
54. Z. Faraji Rad, R. E. Nordon, C. J. Anthony, L. Bilston, P. D. Prewett, J. Y. Arns, C. H. Arns, L. Zhang, G. J. Davies, High-fidelity replication of thermoplastic microneedles with open microfluidic channels. *Microsyst. Nanoeng.* **3**, 17034 (2017).
55. K. Z. Huang, Z. L. Xu, I. King, M. R. Lyu, C. Campbell, Supervised self-taught learning: Actively transferring knowledge from unlabeled data, in *IEEE International Joint Conference on Neural Network (14 to 19 June 2009)*, pp. 481.
56. A. Quattoni, M. Collins, T. Darrell, Transfer learning for image classification with sparse prototype representations, in *Proceedings of IEEE Conference on Computer Vision and Pattern Recognition (IEEE, 2008)*, pp. 2300–2307.
57. S. Y. Tzeng, R. Guarecuco, K. J. McHugh, S. Rose, E. M. Rosenberg, Y. Zeng, R. Langer, A. Jaklenec, Thermostabilization of inactivated polio vaccine in PLGA-based microspheres for pulsatile release. *J. Control. Release* **233**, 101–113 (2016).
58. P. M. Allen, M. G. Bawendi, Ternary I-III-VI quantum dots luminescent in the red to near-infrared. *J. Am. Chem. Soc.* **130**, 9240–9241 (2008).
59. L. H. Jing, S. V. Kershaw, Y. Li, X. Huang, Y. Li, A. L. Rogach, M. Gao, Aqueous Based Semiconductor Nanocrystals. *Chem. Rev.* **116**, 10623–10730 (2016).
60. L. A. Li, A. Pandey, D. J. Werder, B. P. Khanal, J. M. Pietyga, V. I. Klimov, Efficient synthesis of highly luminescent copper indium sulfide-based core/shell nanocrystals with surprisingly long-lived emission. *J. Am. Chem. Soc.* **133**, 1176–1179 (2011).
61. P. Reiss, M. Protière, L. Li, Core/Shell semiconductor nanocrystals. *Small* **5**, 154–168 (2009).
62. Computer code associated with Biocompatible near-infrared quantum dots delivered to the skin by microneedle patches to record vaccination; doi.org/10.5281/zenodo.3571386.

Acknowledgments: We acknowledge W. H. Gates, D. Hartman, S. Hershenson, S. Kern, B. Nikolic, K. Owen, L. Shackelton, C. Karp, and D. Robinson for their guidance; R. T. Bronson for pathology expertise; and the MIT Department of Comparative Medicine for advice. We thank W. Weldon and his laboratory at the U.S. Centers for Disease Control and Prevention for performing neutralizing antibody titer studies, the Koch Institute Swanson Biotechnology Center for technical support, specifically the Hope Babette Tang (1983) Histology Facility and the Peterson (1957) Nanotechnology Materials Core Facility as well as the Harvard University Center for Nanoscale Systems, and W.M. Keck Microscopy Facility at the Whitehead Institute.

Funding: This work was funded by the Bill & Melinda Gates Foundation grant OPP 1150646. Fellowship support for K.J.M. was provided by an NIH Ruth L. Kirschstein National Research Service Award (F32EB022416). L.J. thanks the Youth Innovation Promotion Association CAS (2018042), National Natural Science Foundation of China (81671755), and China Scholarship Council (201604910444) for financial support. This work was supported in part by the Koch Institute Support (core) Grant P30-CA14051 from the National Cancer Institute. This work was performed in part at the Harvard University Center for Nanoscale Systems (CNS), a member of the National Nanotechnology Coordinated Infrastructure Network (NNCI), which is supported by the National Science Foundation under NSF award no. 1541959. **Author contributions:** K.J.M., R.L., A.J., L.W., and P.A.W. devised the concept. K.J.M., L.J., R.L., and A.J. designed the experiments and wrote the manuscript. L.J. designed and synthesized QDs. L.J., H.S.N.J., C.F.P., and J.Y. performed optical characterization and analysis. M.G.B. and M.G. oversaw QD synthesis and analysis. L.J., H.S.N.J., and W.T. performed QD encapsulation. M.S. performed the computational modeling simulations. K.J.M., S.Y.S., and M.C. designed and fabricated microneedles. K.J.M., S.Y.S., C.F.P., F.L., M.P., N.P., and A.K. designed the smartphone optics. K.J.M., L.J., H.S.N.J., S.Y.S., S.Y.T., T.G., J.C., J.L.S., and M.T. performed the in vitro experiments. K.J.M., S.Y.S., and M.C. performed the ex vivo studies. K.J.M., S.Y.S., M.C., S.R., and S.T. performed the in vivo experiments and corresponding analysis. M.S. and D.V. developed the machine learning algorithm. **Competing interests:** A patent application entitled “Microneedle tattoo patches and use thereof” describing the approach presented here was filed by K.J.M., L.J., S.Y.S., H.S.N.J., A.J., and R.L. (US 62/558,172). R.L. discloses potential competing interests in the below link: www.dropbox.com/s/yc3xqb5s8s94v7x/Rev%20Langer%20COI.pdf?dl=0.

Data and materials availability: All data associated with this study are present in the paper or the Supplementary Materials. Computer code archive is publicly accessible: doi.org/10.5281/zenodo.3571386.

Submitted 20 July 2019

Accepted 27 November 2019

Published 18 December 2019

10.1126/scitranslmed.aay7162

Citation: K. J. McHugh, L. Jing, S. Y. Severt, M. Cruz, M. Sarmadi, H. S. N. Jayawardena, C. F. Perkinson, F. Larusson, S. Rose, S. Tomasic, T. Graf, S. Y. Tzeng, J. L. Sugarman, D. Vlastic, M. Peters, N. Peterson, L. Wood, W. Tang, J. Yeom, J. Collins, P. A. Welkhoff, A. Karchin, M. Tse, M. Gao, M. G. Bawendi, R. Langer, A. Jaklenec, Biocompatible near-infrared quantum dots delivered to the skin by microneedle patches record vaccination. *Sci. Transl. Med.* **11**, eaay7162 (2019).

Biocompatible near-infrared quantum dots delivered to the skin by microneedle patches record vaccination

Kevin J. McHugh, Lihong Jing, Sean Y. Severt, Mache Cruz, Morteza Sarmadi, Hapuarachchige Surangi N. Jayawardena, Collin F. Perkinson, Fridrik Larusson, Sviatlana Rose, Stephanie Tomasic, Tyler Graf, Stephany Y. Tzeng, James L. Sugarman, Daniel Vlastic, Matthew Peters, Nels Peterson, Lowell Wood, Wen Tang, Jihyeon Yeom, Joe Collins, Philip A. Welkhoff, Ari Karchin, Megan Tse, Mingyuan Gao, Mounji G. Bawendi, Robert Langer and Ana Jaklenec

Sci Transl Med **11**, eaay7162.
DOI: 10.1126/scitranslmed.aay7162

On the record

Vaccines prevent disease and save lives; however, lack of standardized immunization recordkeeping makes it challenging to track vaccine coverage across the world. McHugh *et al.* developed dissolvable microneedles that deliver patterns of near-infrared light-emitting microparticles to the skin. Particle patterns are invisible to the eye but can be imaged using modified smartphones. By codelivering a vaccine, the pattern of particles in the skin could serve as an on-person vaccination record. Patterns were detected 9 months after intradermal delivery of microparticles in rats, and codelivery of inactivated poliovirus led to protective antibody production. Discrete microneedle-delivered microparticle patterns in porcine and pigmented human skin were identifiable using semiautomated machine learning. These results demonstrate proof of concept for intradermal on-person vaccination recordkeeping.

ARTICLE TOOLS

<http://stm.sciencemag.org/content/11/523/eaay7162>

SUPPLEMENTARY MATERIALS

<http://stm.sciencemag.org/content/suppl/2019/12/16/11.523.eaay7162.DC1>

RELATED CONTENT

<http://stm.sciencemag.org/content/scitransmed/11/503/eaaw3329.full>
<http://stm.sciencemag.org/content/scitransmed/10/467/eaar2227.full>

REFERENCES

This article cites 55 articles, 1 of which you can access for free
<http://stm.sciencemag.org/content/11/523/eaay7162#BIBL>

PERMISSIONS

<http://www.sciencemag.org/help/reprints-and-permissions>

Use of this article is subject to the [Terms of Service](#)

Science Translational Medicine (ISSN 1946-6242) is published by the American Association for the Advancement of Science, 1200 New York Avenue NW, Washington, DC 20005. The title *Science Translational Medicine* is a registered trademark of AAAS.

Copyright © 2019 The Authors, some rights reserved; exclusive licensee American Association for the Advancement of Science. No claim to original U.S. Government Works

Supplementary Materials for

Biocompatible near-infrared quantum dots delivered to the skin by microneedle patches record vaccination

Kevin J. McHugh, Lihong Jing, Sean Y. Severt, Mache Cruz, Morteza Sarmadi, Hapuarachchige Surangi N. Jayawardena, Collin F. Perkinson, Fridrik Larusson, Sviatlana Rose, Stephanie Tomasic, Tyler Graf, Stephany Y. Tzeng, James L. Sugarman, Daniel Vlastic, Matthew Peters, Nels Peterson, Lowell Wood, Wen Tang, Jihyeon Yeom, Joe Collins, Philip A. Welkhoff, Ari Karchin, Megan Tse, Mingyuan Gao, Mounji G. Bawendi, Robert Langer*, Ana Jaklenec*

*Corresponding author. Email: rlanger@mit.edu (R.L.); jaklenec@mit.edu (A.J.)

Published 18 December 2019, *Sci. Transl. Med.* **11**, eaay7162 (2019)
DOI: 10.1126/scitranslmed.aay7162

The PDF file includes:

Materials and Methods

Fig. S1. Optical properties of organic dyes.

Fig. S2. Evolution of fluorescence emission properties with shelling time.

Fig. S3. Fluorescence lifetime characterization of the S10C QD series.

Fig. S4. Composition and physical properties of S10C5H QDs.

Fig. S5. pH stability of PMMA-encapsulated QDs.

Fig. S6. Finite element analysis of mechanical forces on microneedles.

Fig. S7. Optimization of microneedle geometry using finite element analysis.

Fig. S8. Machine learning training and validation.

Table S1. Spectral characterization of custom QD formulations.

Table S2. Multiexponential fitting parameters for photoluminescence decay curves.

Legend for movie S1

References (54–62)

Other Supplementary Material for this manuscript includes the following:

(available at stm.sciencemag.org/cgi/content/full/11/523/eaay7162/DC1)

Movie S1 (.mp4 format). Intradermal administration and imaging of encapsulated QDs.

Data file S1 (Microsoft Excel format). Individual subject-level data.

Materials and Methods

Materials and reagents

All chemicals used to synthesize and encapsulate quantum dots (QDs) and form microneedles were purchased from Sigma-Aldrich with the exception of copper (I) iodide, indium (III) acetate, oleic acid purchased from Alfa Aesar, poly(vinyl alcohol) (PVA) purchased from Polysciences, and SYLGARD 184 silicone elastomer (polydimethylsiloxane) purchased from Dow Chemical Company. Alexa Fluor 790 succinimidyl ester and DyLight 800 NHS ester were purchased from Thermo Fisher Scientific. IRDye 800CW was purchased from LI-COR Biosciences. IR-820 was purchased from Sigma-Aldrich. Sulfo-Cyanine7 NHS ester was purchased from Lumiprobe. VivoTag 800 was purchased from PerkinElmer. Indocyanine green was purchased from MP Biomedicals. IRDC2 and IRDC3 were purchased from LDP LLC.

Fluorophore characterization

Steady-state photoluminescence (PL) spectra were measured using a SpectraPro-300i single-grating spectrometer (Princeton Instruments) in conjunction with a DET10N single-channel indium gallium arsenide (InGaAs) detector (Thorlabs). All steady-state PL measurements were conducted using 532 nm laser excitation, and emission was collected using a pair of gold-coated off-axis parabolic mirrors. The photoluminescence quantum yield (PL QY) of the QDs was obtained using an RTC-060-SF integrating sphere (Labsphere). The PL QY was measured using 405 nm laser excitation. QDs chosen for further study were also evaluated under 808 nm laser excitation. Color glass long-pass filters were used to block the excitation beam. The light output from the integrating sphere was detected using a calibrating 818-IR germanium detector (Newport) through a SR830 lock-in amplifier (Stanford Research Systems). The sample was placed in a polytetrafluoroethylene-capped quartz cuvette, and a solvent blank was used to ensure that the environment inside the sphere was as uniform as possible. The measured photocurrent was adjusted to account for the external quantum efficiency of the detector when calculating the PL QY. The measured PL QY was then corrected to account for leakage of the excitation light and the transmittance of the filter. Lastly, time-resolved PL decay was measured using an LDH-P-FA-530B spectrometer (PicoQuant) equipped with a picosecond pulsed diode laser (pulse width: 100 ps) as a single wavelength excitation source (532 nm) for time-correlated single-photon counting measurements.

Transmission electron microscopy (TEM) and high-resolution TEM images were recorded on a FEI TECNAI G2 SPIRIT TWIN operating at 120 kV and a JEOL JEM-2010F microscope operating at 200 kV, respectively. The elemental composition of S10C5H QDs was analyzed using energy-dispersive X-ray (EDX) spectroscopy. Prior to measurement, QDs were rinsed with a 1:3 ratio of water-to-isopropanol and filtered using Amicon 3 kDa desalting filters (EMD Millipore) to remove byproducts and oleic acid. Approximately 20 μ L of the resulting solution was placed on a nickel-coated TEM grid and dried under ambient conditions. Elemental measurements were then made using a JEOL JEM-2010F microscope.

Fabrication of core/shell and its impact on the optical properties of QDs

Ternary I-III-VI semiconductor nanocrystals or quantum dots (QDs), such as near-infrared (NIR) emitting copper indium selenide (CISE) QDs presented here, are attractive alternatives to the more well-studied Cd-, Pb-, or Hg-containing QDs for in vivo imaging applications (27, 54). In

addition to avoiding potential toxicity from cadmium and lead ions, these QDs can also be excited and emit in the NIR where penetration through biological tissue is favorable. However, the PL QY of I-III-VI QDs cores is typically low (<10%). It has been demonstrated that coating QDs with epitaxially-grown wide-bandgap semiconducting materials is a very efficient means to electronically passivate the QD surface for boosting the PL QY and achieving better stability against photobleaching (55-57). Zinc sulfide (ZnS), a non-toxic, stable, and abundant semiconducting material, was chosen to overcoat the as-prepared CISE cores due to its large bandgap ($E_{g,bulk} \sim 3.61$ eV), which provides a type I band alignment with CISE ($E_{g,bulk} \sim 1.05$ eV). Furthermore, the lattice mismatch between ZnS and CISE is around 7%, thereby enabling the epitaxial growth of ZnS shell without introducing intensive strain on the cores and thus high PL QY. In some QD formulations, aluminum ions were also introduced into ZnS lattice during shell growth in order to further enhance long-term photostability against oxidation. It was previously found Al doped in the CdS shell on CdSe cores formed into aluminum oxide, which can serve as a self-passivation layer on the surface of the core/shell QDs and effectively enhance photostability (50). Therefore, aluminum doped ZnS shells were designed to enhance the resistance to photodegradation under harsh and/or long-term light irradiation.

Typical temporal evolutions of optical properties of CuInSe₂ cores by using stoichiometric ratio and shell growth are shown in **Fig. 2, B** and **C**, and **figs. S2** and **S3**. In **Fig. 2B** and **fig. S2A**, a 1 h shelling reaction leads to an obvious blue shift of the PL emission peak from 964 nm to 916 nm, and when the coating reaction was prolonged, the position of PL emission only slightly changed (further blue-shifted to 891 nm after 5 h). The initial blue shift or increase of the quantum confinement was resulted from the shrinkage in the emissive core size, likely due to near-surface Zn interdiffusion. This cannot be attributed to the further growth or ripening of the CISE cores, although unpurified CISE cores were directly used as seeds for further shell growth in the presence of excess of CISE precursors. The spectroscopic observations in the late stages of reaction strongly suggests that the distinct epitaxial shell coating process is dominant over Zn²⁺ indiffusion, which serves as a protective barrier surrounding the core and accounts for the further PL enhancement. As shown in **Fig. 2C**, 1 h of shelling time resulted in an obvious increase in PL QY, (16.2% to 27.6%) when excited at 405 nm due to initial surface passivation. Afterwards, PL QY further increased with prolonged shell growth time, reaching to 43.6% (λ_{ex} : 405 nm) and 31.3% (λ_{ex} : 808 nm) after 5 h of shell growth.

CuInSe₂ has the chalcopyrite structure which is a slightly modified form of zinc blende, where Cu⁺ and In³⁺ ions occupy the Zn²⁺ positions, similar to the case of CuInS₂ (51). Zn²⁺ ions readily diffuse into the CuInSe₂ lattice due to the small difference of ionic radii between Zn²⁺ and Cu⁺. Therefore, the initial PL shifts can be attributed to the Zn²⁺ indiffusion into near-surface lattice of CISE core. As a consequence, the radiative transition of the conduction band involving Zn²⁺ to internal defect levels occurs. The formation of Zn graded core and etched cores prior to surface epitaxial shell coating has been shown to account for a similar phenomenon during the initial shelling stage of CuInS₂ (51), resulting in both an increase the band gap of starting fluorescent center due to the wider band gap of bulk ZnS than that of CISE. In the meantime, the observed narrowing of PL full width at half maximum (FWHM) against shell growth suggests that an annealing process of the CISE incorporated with Zn²⁺ ions and simultaneous ZnS shell growth did not give rise to either size or composition distribution broadening for the particles in the ensemble (**fig. S2**).

To further confirm the presence of the shell structure, the time-resolved PL (TRPL) measurements were performed to reveal the nature and influence of various surface states

involved in the emission processes. The PL decay curves measured at the PL emission peak (λ_{max}) are shown in **fig. S3A**. In general, the PL relaxations of the CISE seeds and their core/shell QDs were characterized by multi-exponential processes that were best fit by three-exponential decays (all decay fitting data are summarized in **table S2**). The average lifetime of the entire fluorescence decay process was further determined from these three-exponential decay fits (**fig. S3 inset**). The entire recombination process of the initial CISE core particles was comprised of three decay components with time constants of 4.1 ns, 55.1 ns, and 218.5 ns as shown in **table S2**. The origin of PL emission in ternary I-III-VI nanocrystals is not fully understood, but may involve surface defect-related recombination, conduction band to internal defect recombination, and donor-acceptor pair recombination processes. The fitting data suggest the first recombination channels for CISE core emission (the surface defect related recombination) is partially suppressed with its component amplitude (B_1) decreasing from 35.0% to 26.5% after 5 h of shelling. This suggests the shell coating suppresses the fast decay channel by inhibiting the effects of the surface state on emission while recombination from the conduction band to internal defects was enhanced with the component amplitude increasing from 22.8% to 34.6% (B_2). The lifetime associated with this fast decay slightly increases from 4.1 ns to 4.7 ns indicating a reduction of the recombination rate via this channel and so the fast component contribution was slightly decreased, going from 1.7% to 1.5% of the overall emitted fluorescence. A more substantial impact of shelling is seen in the changes to the second decay process with regards to the conduction band to internal defect recombination. Here the emission linked to this process increases in both amplitude and lifetime, resulting in a net increase in PL emission from 14.9% to 25.8%. This increase is seen as evidence of the aforementioned diffusion of Zn into the core surface lattice, filling defects (vacancies) and thereby healing them. Furthermore, in contrast to the second term, the third terms associated with donor-acceptor related recombination diminishes in terms of lifetime as well as its net contributions to emission, from 252.1 ns to 183.2 ns, and from 83.4% to 72.7%, respectively. This suggests that the Cu-related internal defects largely accounting for the third slow recombination process were decreased by Zn interdiffusion to core. As a result, the average lifetime presents a decreasing trend against shell growth time as shown in the inset of **fig. S3A**. However, this recombination channel still dominated the whole emission process, suggesting the nature of the emission of CISE core QDs was maintained and internal defects at the origin of the PL emission are located inside the CISE cores.

The recombination rates derived from transient PL spectroscopy are plotted against shell growth time in **fig. S3B**. A larger increase for radiative recombination rate is observed against shell growth time, while the non-radiative recombination rate remained nearly unchanged. In principle, if the radiative recombination rate is increased when forming a heterostructure, it is necessary to suppress the increase in the non-radiative recombination rate to obtain high PL QY. Therefore, the overgrowth of the shell with a wider band gap ZnS-based materials reported herein effectively prevents exciton trapping at surface states, which are largely responsible for the quality of resulting core/shell interfaces formed during the shelling reaction, thereby presenting an increasing tendency in the ensemble PL QY against shell growth. In absolute terms, these relative changes give rise to an overall improvement in the PL QY, from a core QD PL QY of around 16.2% to a core/shell QD with lowered defect levels having a PL QY of around 43.6%. All these variations support the presence of an outer ZnS shell structure proposed above, with some indiffusion of Zn into the core. Therefore, the CISE core most likely transitions to a Zn gradient structure before reaching a ZnS outer shell.

The PL decay curves were fitted using a multi-exponential function:

$$I(t) = \sum_{i=1}^n B_i \exp(-t/\tau_i), \quad \sum_{i=1}^n B_i = 1 \quad (\text{S1})$$

In this expression, τ_i represent the decay time constants, and B_i represents the normalized amplitude of each component, n is the number of decay times. Because the photoluminescence decays for all the QDs are best fitted using a two-/three-exponential model ($n = 2/3$), the amplitude weighted average decay lifetime τ_{avg} of the entire fluorescence decay process was calculated with the form:

$$\tau_{\text{avg}} = \frac{\sum B_i \tau_i^2}{\sum B_i \tau_i} \quad (\text{S2})$$

The normalized lifetime-amplitude product is given as:

$$f_i = \frac{\tau_i B_i}{\sum \tau_i B_i} \quad (\text{S3})$$

In this expression, f_i represents the relative time-integrated contribution of each respective process to the overall number of emitted photons (i.e., the emission intensity measured in steady state PL spectra).

In addition, given the experimentally determined PL quantum yield (QY), the radiative recombination lifetime (τ_r) is given as:

$$\tau_r = \frac{\tau_{\text{avg}}}{\text{QY}} \quad (\text{S4})$$

and then the non-radiative recombination lifetimes (τ_{nr}) is given as:

$$\tau_{\text{nr}} = \frac{1}{(1/\tau_{\text{avg}} - 1/\tau_r)} \quad (\text{S5})$$

The PL decay-fitting data for all curves are summarized in **table S2**.

Computational modeling of microneedle geometry

COMSOL Multiphysics was used to perform finite element analysis on various microneedle shapes. Microneedle structure was numerically modeled using a linear elastic constitutive material model with an elastic modulus of 1.7 GPa in accordance with data obtained from tensile testing experiments (1.7 ± 0.3 GPa, $n = 8$) and Poisson's ratio of 0.45. The Structural Mechanics Module was used to run simulations with a physically-controlled, extra fine mesh size. The geometries explored included a cone, cylinder, and intermediate portions thereof in which the lower portion of the microneedle was a cylinder and the upper portion of the microneedle was a cone. Microneedle height was fixed at 1500 μm . As a result, the shape could be fully defined by two parameters: microneedle diameter and alpha, which represented the proportion of the microneedle height that was cylindrical.

Fifty distinct microneedle designs with microneedle diameter ranging from 100 μm to 300 μm and alpha varying from 0 to 0.9 were evaluated for six criteria: critical load factor under buckling, displacement under axial loading, von Mises stress under axial loading, displacement under bending, von Mises stress under bending, and theoretical deliverable volume at the microneedle tip. Buckling measurements were performed based on a method previously reported

(30). Briefly, the microneedle tip was fully constrained and a total downward load of 5 N was applied to the base center while the microneedle was free to move only along the shaft axis. To perform axial loading simulations, a pressure of 3.18 MPa, equal to the skin penetration stress (58), was applied to the tapered region in an axial direction (along the shaft). Bending simulations were conducted by applying a total lateral load of 20 mN to the tapered region, similar to a method previously reported (59). All degrees of freedom of the microneedle base were fully constrained in both axial and bending loading analyses. Maximum von Mises stress and maximum displacement in the structure were obtained from axial and bending load analysis while critical buckling load—representing the stability of structure against buckling—was calculated from buckling analysis. Based on these analyses, we generated dissolvable needles with favorable properties for skin penetration and deliverable volume.

Microneedle mold fabrication

Microneedle arrays were designed using Sketchup Make (Trimble Inc.) and exported as stereolithography (.stl) files. These computer-aided design files were then opened in DeScribe (Nanoscribe GmbH), sliced, and hatched using adaptive slicing with a minimum slicing distance of 0.1 μm , shell and scaffold printing with a 1 μm hatching distance, shell contour count of 6, base slice count of 12, and 1 μm hatching distance with a triangular interior scaffold and power setting of 50,000. The exported files were then loaded into NanoWrite and printed using a Nanoscribe to perform dip-in laser lithography with a 25x objective lens in IP-S atop glass coated with indium tin oxide. After the print had completed, unexposed IP-S was removed by soaking the slide in propylene glycol methyl ether acetate for 10 min and then soaking in isopropanol for 10 additional min.

Photoresist master molds were then coated with a thin layer of trichloro(1H,1H,2H,2H-perfluorooctyl) silane by placing the mold alongside a glass slide covered with the chemical in a desiccator under house vacuum for 1 hour. The mold was then fixed to the bottom of a petri dish using double-sided tape and covered with polydimethylsiloxane (PDMS, Sylgard 184, Dow Corning) mixed according to the manufacturer's instructions, and placed overnight in an oven at 60°C. The cross-linked PDMS was then removed from the photoresist mold and subsequently used to create mater mold replicates or dissolvable microneedles. To create additional mater molds, the UV-curable Norland Optical Adhesive 61 was filled into the PDMS molds using a centrifuge at 3,234 RCF for 5 min placed in a UV-curing oven at room temperature for 15 min and manually removed by attaching a small piece of glass to the backing of the patch using double-sided tape.

Mechanical testing of microneedles

The force required to penetrate synthetic human skin (SynDaver) or explanted porcine skin was evaluated using a Dynamic Mechanical Analyzer Q800 (TA Instruments) in compression mode. Microneedle arrays composed of Norland Optical Adhesive 61 (Norland Products) were used to prevent complications due to dissolution. Microneedle patches were inverted and affixed to the top platform of the compression clamp using double-sided tape while skin was placed on the bottom compression platform. An initial pre-load force of 2.5 mN was applied to bring the needle tips into contact with the skin. Force was then applied to determine the amount required to penetrate the skin surface. Visual inspection was used rather than displacement because of the propensity of the skin sample to compress. A minimum force step of 2.5 mN was used to determine the minimum penetration force required. 3x3 arrays of each microneedle geometry

tested were analyzed using three trials each in different areas of the skin sample. Studies evaluating the effect of needle spacing utilized 3x3 arrays of the optimized microneedle shape (750/750 μm cylinder/cone) at a spacing of 900 μm or 3233 μm .

In vitro evaluation of quantum dot toxicity

The in vitro toxicity of QDs with a copper indium selenide core and aluminum-doped zinc sulfide shell was evaluated in mouse macrophages (Raw 264.7 cells) and compared to PMMA-encapsulated QDs and commercial lead sulfide (PbS) core-type QDs with an oleic acid coating (Sigma-Aldrich). Prior to plating cells, samples were plated onto 96-well glass bottom plates (Cellvis) in 100 μL of either toluene for hydrophobic unencapsulated QDs or sterile water for PMMA-encapsulated QDs at 1000, 200, 40, and 8 $\mu\text{g/ml}$. After drying, cells were plated at 10,000 cells/well in 100 μL of phenol red-free DMEM (Life Technologies) supplemented with 10% fetal bovine serum and 1% penicillin/streptomycin and incubated at 37°C in 5% CO_2 for 24 hours. Cell viability was then determined using a CellTiter-Glo Luminescent Assay (Promega) according to the manufacturer's instructions.

Ex vivo microneedle application

Microneedle penetration and microparticle delivery was assessed ex vivo in Yorkshire pig skin obtained from the ear and human cadaveric skin donated to the National Disease Research Interchange fulfilled under protocol DLAR9-001. Microneedle patches were imaged before and after administration using a Leica M80 microscope and Leica IC80 HD Camera and scanning electron microscope using the preparation and imaging parameters described above. Tissue samples were also imaged before and after the application of a dissolvable microneedle patch containing PMMA-encapsulated QDs using the adapted smartphone with and without LED illumination and emission filters.

Image processing

After collection, images were downloaded from the phone, cropped to a size of 237x279 in Adobe Photoshop to isolate a single pattern, and saved as portable network graphics (.png) files. These images were then used directly for detection via machine learning. For signal quantification in longitudinal imaging studies, cropped images were further split into three constituent red, green, and blue channels in ImageJ and the red channel was saved as a grayscale image. For signal-above-background quantification in the short-terms study, circular ROIs 80 pixels in area were then manually placed for each of the sixteen markings in the 4x4 array. The average value of the remaining pixels in the image was then subtracted to obtain signal-above-background. SNR was calculated similarly; however, to reduce diffuse light surrounding the NIR markings, which would have a larger effect on SNR, background was calculated by measuring the average intensity of all pixels that fell outside 616-pixel ROIs associated with each marking and then taking the average of all pixels outside of this area. This technique allowed for a compromise between adequately representing the brightness of the signal while eliminating most diffuse, signal-associated brightness that is not representative of the true background. The signal from each marking was then divided by the background signal to generate a SNR. Using smaller signal ROIs or larger ROIs for background subtraction would serve to further increase SNR.

Machine learning detection algorithm

Transfer learning-based machine learning has recently emerged as a promising method for image classification, particularly when there is a lack of sufficient training data (60, 61). Here, we applied this approach to a pre-trained AlexNet neural network, a classification tool with 25 layers (20) tuned to classify three spatial patterns of interest: a circle, cross, and rectangle. The Deep Learning Toolbox model of AlexNet available in MATLAB was used for all image classification. The first 22 layers of AlexNet (1-22), which contained the image segmentation and feature extraction properties, were directly transferred from the original AlexNet. The top three layers (22-25) were modified to classify the three patterns of interest.

To generate a training dataset, 30 images per pattern were selected from animals not included in the test data, which will subsequently be referred to as source images. Image augmentation was then performed on each source image containing an individual pattern by applying a set of modifications using a pre-processing code (62). This code performed a series of functions including image cropping, inversion, and rotation, brightness normalization, grayscale conversion, and resizing. The set of 30 modified source images per pattern were each then used to generate 100 augmented image for a total of 3,000 images per pattern (9,000 total). Using this approach, 70% of the generated images were used for training the last three layers of the network while 30% were retained for validation. Rectified Linear Unit (ReLU) was employed as the activation function. A maximum epoch number of 20, minibatch size of 10, and initial learning rate of 1×10^{-4} were selected for training. The training approach was based on labeled and supervised data and resulted in a validation accuracy of 100% after the twentieth epoch (**fig. S8**). Training was performed on a single Nvidia GeForce GTX1080 graphics processing unit and was completed in approximately 2-3 hours.

The trained neural network was then used to classify images from the long-term experimental group receiving QD-loaded microparticles from dissolvable microneedle patches. Images were modified using the same pre-processing method used above prior to their analysis. The classification output consisted of a 3x1 array representing the relative likelihood that the image belonged to each of the trained patterns (circle, cross, or the rectangle). This value was reported as the probability of each classification.

Supplementary Figures:

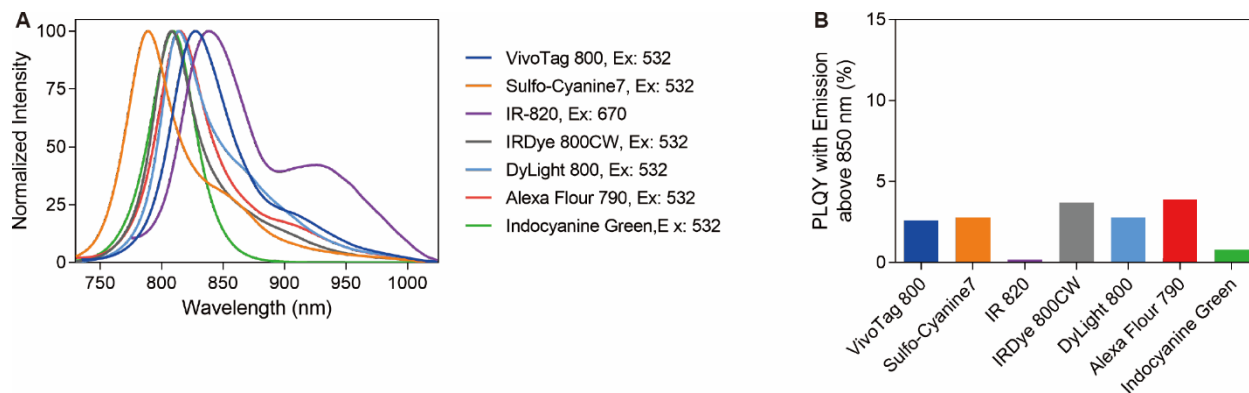


Fig. S1. Optical properties of organic dyes. (A) Emission profiles of NIR organic fluorophores. **(B)** PL QY of NIR organic dyes considering only emission above 850 nm upon excitation at 780 nm.

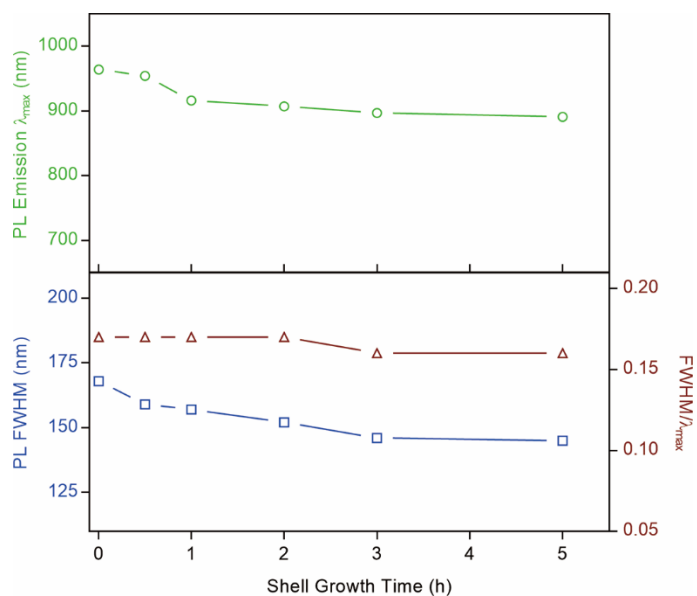


Fig. S2. Evolution of fluorescence emission properties with shelling time. Graphs showing the change in PL emission peak maximum (λ_{\max}) with shelling time (top), full width at half maximum (FWHM) of PL peaks (bottom, squares), and FWHM/ λ_{\max} (bottom, triangles) for the S10C series of QDs, which includes S10C5H, the QD used for all in vivo studies.

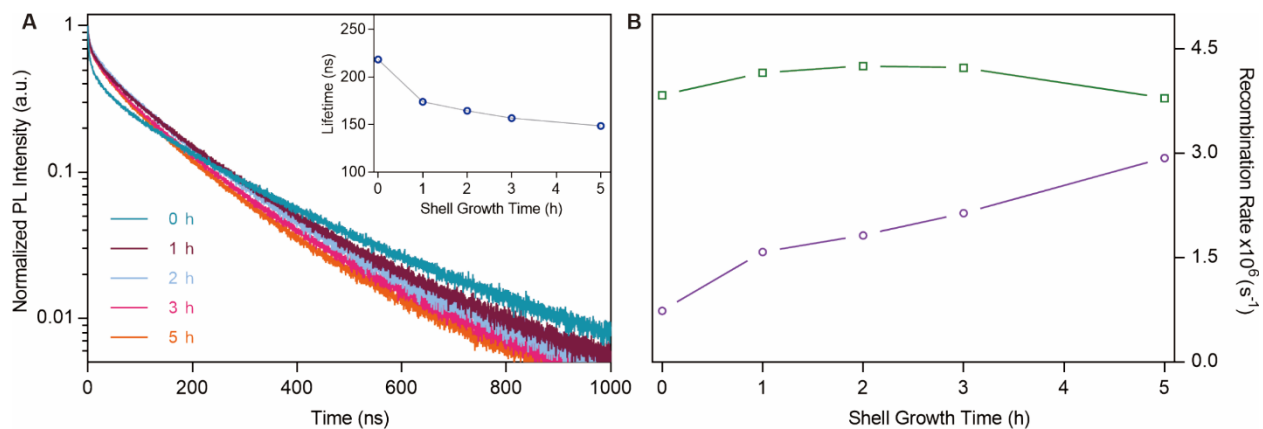


Fig. S3. Fluorescence lifetime characterization of the S10C QD series. (A) Normalized time-resolved PL decay curves together with (inset) corresponding time-resolved PL average lifetimes and (B) radiative (purple circles) and non-radiative (green squares) recombination rates as a function of shell growth time for S10C series.

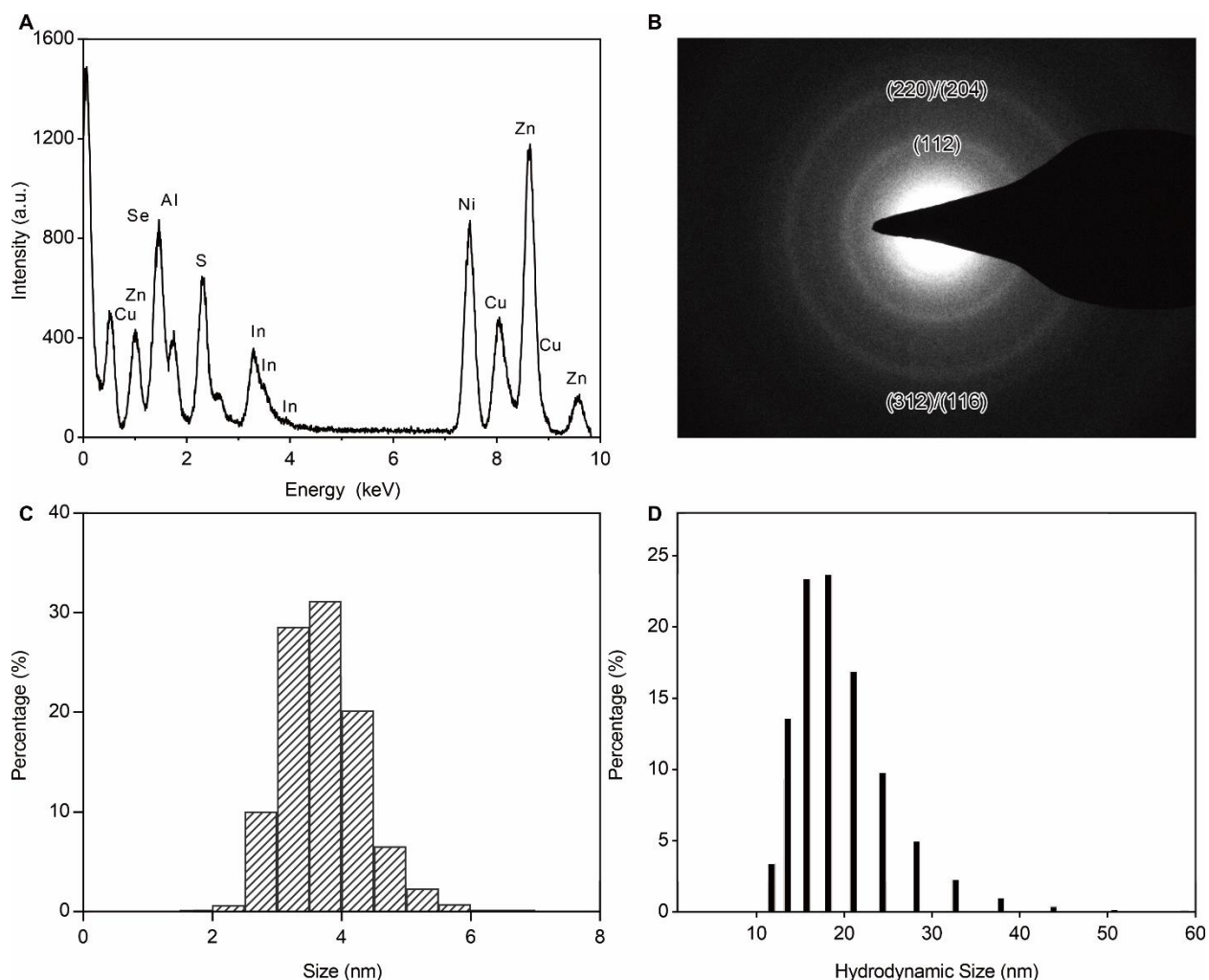


Fig. S4. Composition and physical properties of S10C5H QDs. (A) Energy-dispersive X-ray spectrum and annotated atomic composition of S10C5H QDs. Ni was detected due to the TEM grid substrate. (B) Selected area electron diffraction (SAED) pattern of S10C5H QDs. The well-resolved SAED pattern confirm the chalcopyrite (tetragonal) phase structures, which is the stable phase of bulk CuInSe_2 at room temperature (JCPDS 40-1487). (C) TEM size histogram of S10C5H QDs. (D) Hydrodynamic size histogram of S10C5H QDs dispersed in dichloromethane.

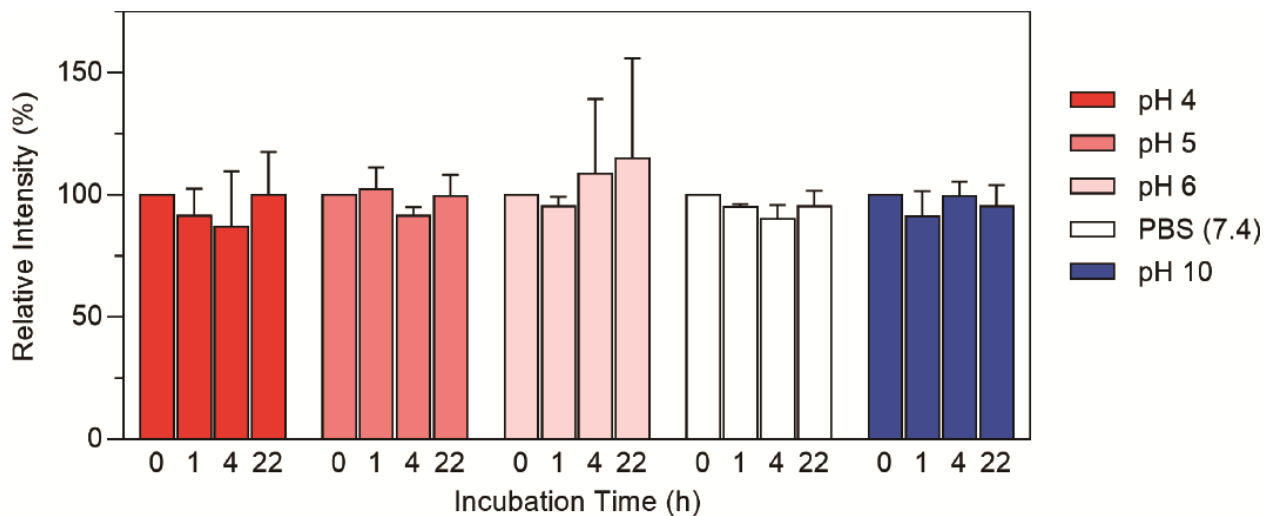


Fig. S5. pH stability of PMMA-encapsulated QDs. The fluorescence intensity of encapsulated S10C5H QDs was compared before and after 22 hours of incubation at pH 4 to 10. $n = 4-5$, $P > 0.05$ for all pH values tested using a two-way ANOVA with Tukey's multiple comparisons test.

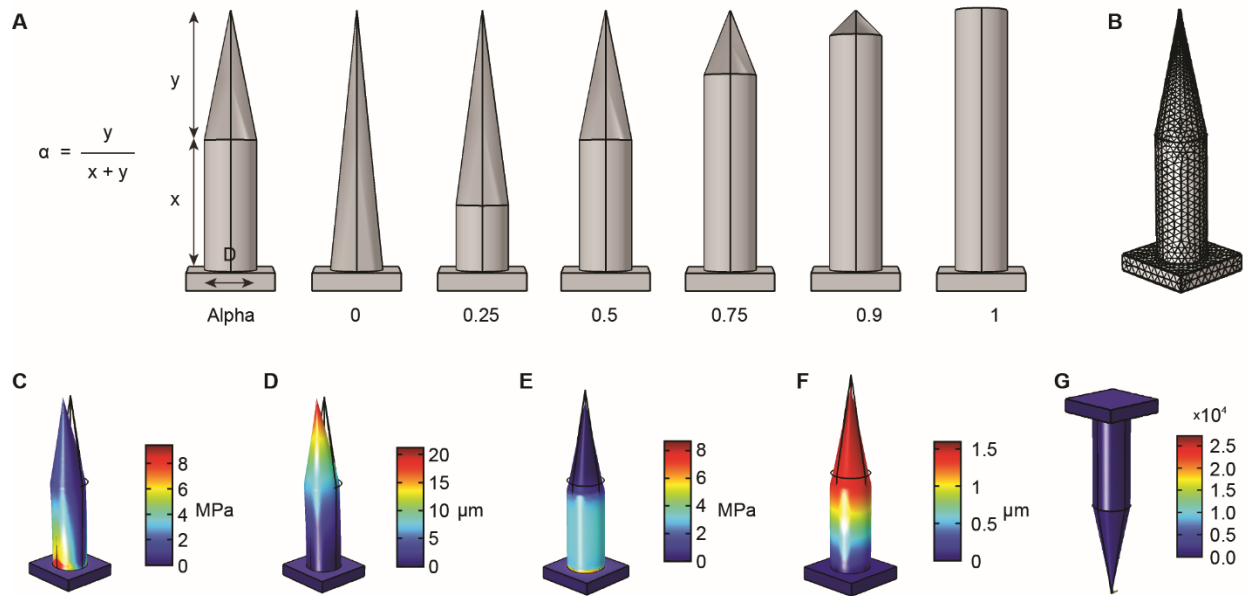


Fig. S6. Finite element analysis of mechanical forces on microneedles. (A) Microneedle shape was modeled in silico with shapes ranging from a cone to a cylinder. (B) Finite element analysis was used to assess the mechanical forces applied during microneedle penetration. Distribution of (C) von Mises stress during bending, (D) displacement during bending, (E) von Mises stress under axial load, (F) displacement under axial load, and (G) total displacement for the optimized design ($\alpha = 0.5$, $D = 300 \mu\text{m}$).

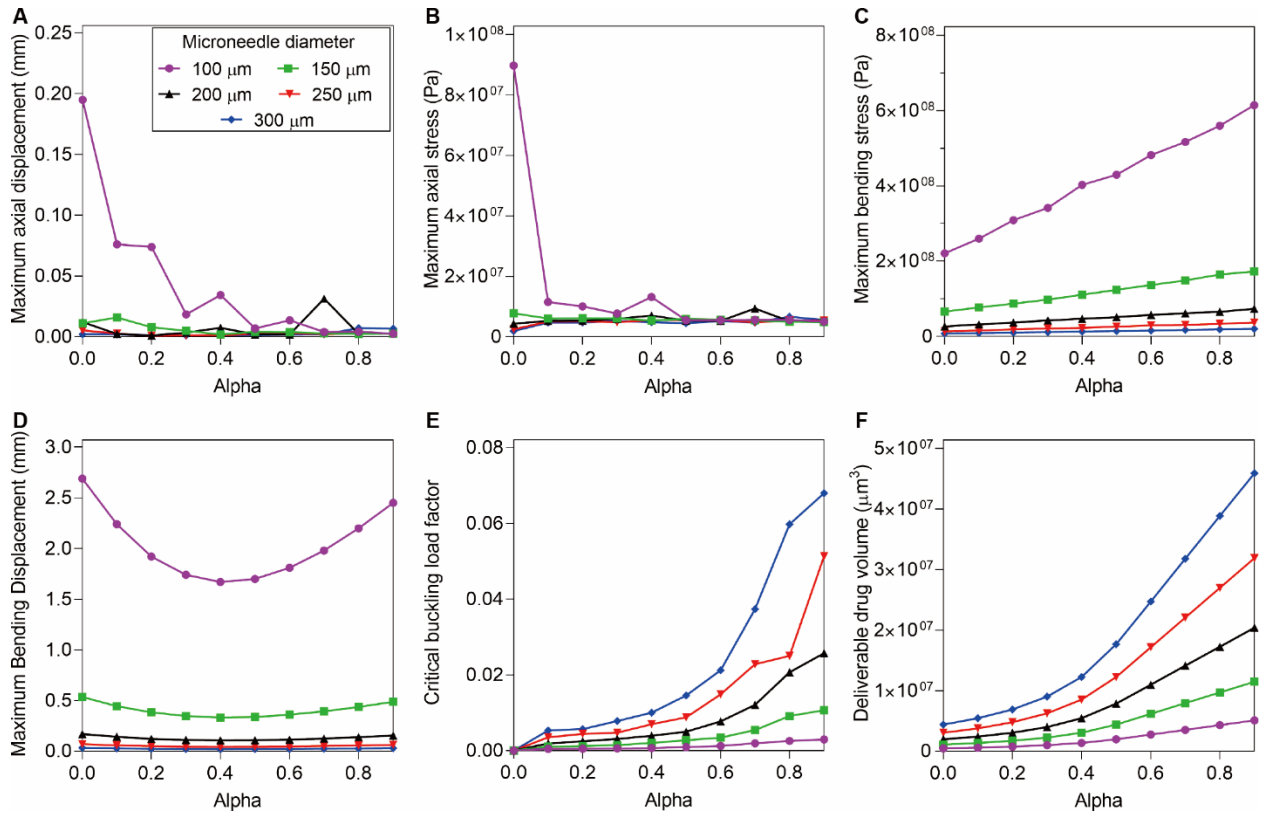


Fig. S7. Optimization of microneedle geometry using finite element analysis. FEA-based optimization of the microneedle geometry was performed regarding six criteria based on microneedle diameter and alpha (the proportion of microneedle height that was cylindrical). **(A)** maximum von Mises stress under axial loading, **(B)** maximum displacement under axial loading, **(C)** maximum von Mises stress under bending, **(D)** maximum displacement under bending, **(E)** critical load factor under buckling, and **(F)** theoretical deliverable drug volume, calculated as the volume of top half of the solid microneedle. In total, 50 geometries were evaluated with shaft diameter ranging from 100 to 300 μm , and alpha ranging from 0 to 0.9.

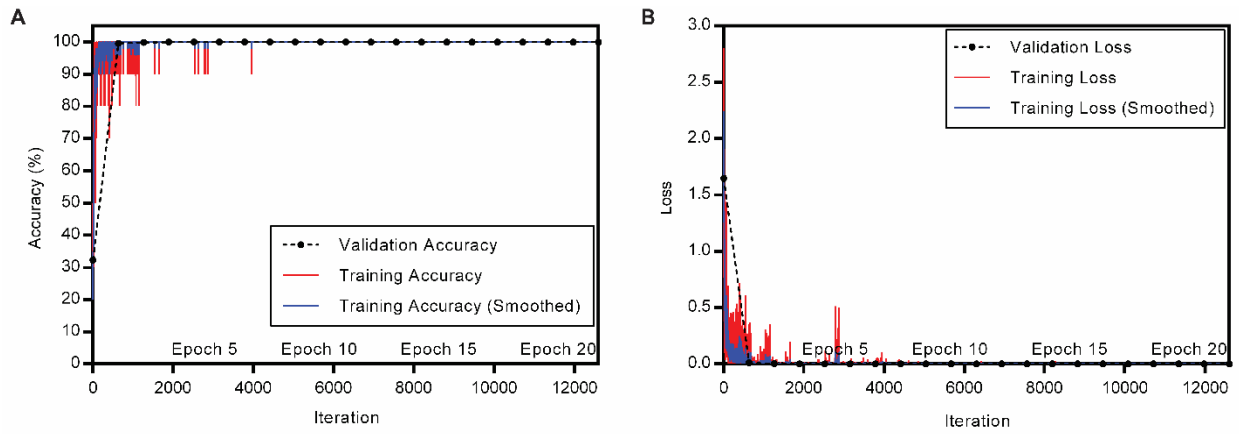


Fig. S8. Machine learning training and validation. Training and validation results of the modified AlexNet network. The resulting validation accuracy after 20 epochs was obtained as 100%, and the loss went to 0.

Supplementary Tables:

Table S1. Spectral characterization of custom QD formulations. The effect of quantum dot composition and shelling time on emission wavelength and quantum yield. Formulations selected for further evaluation highlighted in red.

Formulation	PL Emission Peak (nm)	PL FWHM (nm)	FWHM / Peak	PLQY at 405nm (%)	Cu:In:Se (mol:mol)	[Cu] mol/L	Cu:DDT (mol:mol)	DDT:OLA:OA:ODE (mL:mL)	Zn:Al (mol:mol)	Shelling Time
S2C1.5H	981	187	0.19	37.1±0.1	1:1:2	0.038	1:12	1:0.67:0.33:6.67	1:0	1.5 h
S2C2H	981	175	0.18	35.4±0.1						2 h
S3C2H	981	181	0.18	31.0±0.2	1:1:2	0.038	1:12	1:0.67:0.33:6.67	1:0.3	2 h
S4C1H	750	135	0.18	28.3±0.1	1:4:10	0.013	1:67	1:0.6:0.06:3	1:0.3	1 h
S4C2H	750	141	0.19	36.5±0.1						2 h
S5C0.5H	835	157	0.19	29.5±0.2	1:2:6	0.021	1:40	1:0.6:0.06:3	1:0.3	0.5 h
S5C1H	840	151	0.18	28.3±0.1						1 h
S5C2H	820	145	0.18	36.5±0.1						2 h
S5C3H	810	143	0.18	38.1±0.1						3 h
S8C0H	938	145	0.15	24.2±0.2	1:1.5:2.5	0.029	1:23	1:0.43:0.21:4.29	1:0.3	0 h
S8C1H	895	129	0.14	29.3±0.1						1 h
S8C2H	886	128	0.14	33.9±0.2						2 h
S8C5H	860	127	0.15	41.9±0.2						3 h
S9C0H	1036	244	0.24	10.3±0.0	1:1:2	0.036	1:19	1:0.43:0.21:4.29	1:0	0 h
S9C0.5H	1022	237	0.23	22.5±0.1						0.5 h
S9C1H	1010	245	0.24	9.0±0.03						1 h
S9C3H	1009	219	0.22	21.1±0.1						3 h
S9C5H	968	233	0.24	30.7±0.0						5 h
S10C0H	964	168	0.17	16.2±0.3	1:1:2	0.038	1:12	1:0.67:0.33:6.67	1:0.3	0 h

S10C0.5H	954	159	0.17	37.2±0.1						0.5 h
S10C1H	916	157	0.17	27.6±0.2						1 h
S10C2H	907	152	0.17	30.0±0.2						2 h
S10C3H	897	146	0.16	33.6±0.1						3 h
S10C5H	891	145	0.16	43.6±0.1						5 h
S11C0H	952	141	0.15	26.6±1.3	1:1.5:2.5	0.031	1:15	1:0.67:0.33:6.67	1:0.3	0 h
S11C0.5H	916	134	0.15	38.7±0.4						0.5 h
S11C1H	906	129	0.14	35.4±1.1						1 h
S11C2H	888	124	0.14	40.4±0.6						2 h
S11C3H	879	121	0.14	58.8±2.6						3 h
S11C5H	858	123	0.14	48.7±0.6						5 h
S14C0H	766	132	0.17	21.3±0.6	1:2:3	0.026	1:18	1:0.67:0.33:6.67	1:0	0 h
S14C1H	724	126	0.17	22.2±0.1						1 h
S14C2H	696	124	0.18	37.8±4.8						2 h
S14C3H	680	124	0.18	34.3±0.1						3 h
S14C5H	664	110	0.17	38.3±0.2						5 h
S15C0H	750	131	0.17	19.0±0.3	1:2:3	0.025	1:28	1:0.43:0.09:4.29	1:0	0 h
S15C1H	704	129	0.18	29.1±0.3						1 h
S15C5H	634	145	0.23	42.6±0.1						5 h
S16C0H	880	135	0.15	38.7±0.4	1:2:3	0.024	1:28	1:0.43:0.21:4.29	1:0	0 h
S16C0.5H	878	136	0.15	32.8±0.6						0.5 h
S16C1.5H	860	125	0.15	31.5±1.0						1 h
S16C2H	858	127	0.15	34.6±0.5						2 h
S16C3H	838	130	0.16	37.5±0.2						3 h

S16C5H	812	122	0.15	43.0±0.8						5 h
S17C0H	964	169	0.18	17.3±1.0	1:1:2	0.036	1:19	1:0.43:0.21:4.29	1:0	0 h
S17C0.5H	954	164	0.17	32.5±1.5						0.5 h
S17C1H	940	163	0.17	35.5±0.1						1.5 h
S17C2H	910	160	0.18	38.3±0.9						2 h
S17C3H	902	153	0.17	35.4±0.1						3 h
S17C5H	902	143	0.16	48.4±0.3						5 h
S18C0H	958	167	0.17	15.4±0.1						1:1:2
S18C0.5H	940	152	0.16	33.2±1.1	0.5 h					
S18C1H	918	147	0.16	30.6±0.3	1 h					
S18C2H	904	148	0.16	32.6±0.8	2 h					
S18C3H	894	141	0.16	29.6±0.3	3 h					
S18C5H	884	139	0.16	31.4±0.2	5 h					
S18C7H	886	140	0.16	31.6±0.1	7 h					
S18C18H	878	138	0.16	34.9±0.0	18 h					
S19C0.5H	956	158	0.17	34.6±0.1	1:1:2	0.038	1:12	1:0.67:0.33:6.67	1:0.5	0.5 h
S19C1H	940	159	0.17	28.6±0.3						1 h
S19C2H	920	163	0.18	28.1±0.2						2 h
S19C3H	914	150	0.16	25.7±0.0						3 h
S19C5H	900	145	0.16	28.3±0.2						5 h
S19C7H	886	136	0.15	40.3±0.1						7 h
S19C19H	872	133	0.15	42.0±0.1						19 h
S19C24H	866	136	0.16	41.8±0.2						24 h
S19C48H	874	136	0.16	10.3±0.2						48 h

S19C72H	865	140	0.16	9.1±0.0						72 h
S20C0H	922	136	0.15	23.7±0.7	1:1.5:2.5	0.029	1:23	1:0.43:0.21:4.29	1:0.3	0 h
S20C0.5H	878	127	0.14	25.9±0.4						0.5 h
S20C1H	866	127	0.15	21.3±0.1						1 h
S20C2H	856	126	0.15	31.5±0.5						2 h
S20C3.5H	846	129	0.15	35.9±0.9						3.5 h
S20C5H	828	133	0.16	35.1±0.5						5 h

Note: PL and PL QY data for the S12C and S13C QD series are distorted and likely underestimated due to absorption by the solvent (cyclohexane).

Table S2. Multiexponential fitting parameters for photoluminescence decay curves. The parameters for multi-exponentially fitting the photoluminescence decay curves in fig. S3, normalized amplitude B_i , time constant τ_i and their normalized products f_i , goodness-of-fit parameter χ^2 , together with the detection wavelength.

Sample	λ_{em}^a [nm]	QY ^b [%]	B_1 [%]	f_1 [%]	τ_1 [ns]	B_2 [%]	f_2 [%]	τ_2 [ns]	B_3 [%]	f_3 [%]	τ_3 [ns]	τ_{avg} [ns]	χ^2
0 h (Core)	964	16.2	35.0	1.7	4.1	22.8	14.9	55.1	27.9	83.4	252.1	218.5	0.9992
1 h	916	27.6	26.5	1.4	4.9	33.8	24.2	68.1	33.4	74.4	211.6	174.0	0.9995
2 h	907	30.0	23.8	1.5	5.9	38.9	30.8	74.5	30.5	67.7	209	164.5	0.9995
3 h	897	33.6	27.8	1.3	4.1	33.7	24.3	60.8	32.9	74.4	191	156.9	0.9996
5 h	891	43.6	26.5	1.5	4.7	34.6	25.8	59.7	31.8	72.7	183.2	148.6	0.9997

^a emission peak position, ^b excitation at 405 nm

Supplementary Movies:

Movie S1. Intradermal administration and imaging of encapsulated QDs. Prior to filming rats were anesthetized and a small area of the flank was shaved, treated with depilatory cream, and sterilized using an ethanol swab. The experimental setup included a 780 nm LED illumination source focused on the shaved area of the rat, a NIR-adapted smartphone, a spring-loaded microneedle applicator, and a QD-loaded microneedle patch. Prior to application, no NIR signal was visible on the rat, but was apparent in the microneedle patch. The microneedle patch was then applied for two minutes using the spring-loaded applicator, which transferred QDs into the skin due to dissolution of the microneedle matrix. The transferred QDs were then viewed using the NIR-adapted smartphone to reveal a 4x4 square array.